Thermoacoustic Analysis and Experimental Validation of a Statistically-Based Flame Transfer Function Extracted from Computational Fluid Dynamics

Shrihari Sampathkumar

Thesis submitted to the faculty of the Virginia Polytechnic Institute and State University
in partial fulfillment of the requirements for the degree of

Master of Science
In
Mechanical Engineering

Joseph W. Meadows
Riccardo A. Burdisso
Danesh K. Tafti

July 3, 2019
Blacksburg, Virginia

Keywords: Thermoacoustics, Flame Transfer Function, Combustion, Gas Turbine, Computational Fluid Dynamics

Thermoacoustic Analysis and Experimental Validation of a Statistically-Based Flame Transfer Function Extracted from Computational Fluid Dynamics

Shrihari Sampathkumar

ABSTRACT

Thermoacoustic instabilities arise and sustain due to the coupling of unsteady heat release from the flame and the acoustic field. One potential driving mechanism for these instabilities arise when velocity fluctuations (u') at the fuel injection location causes perturbations in the local equivalence ratio and is convected to the flame location generating an unsteady heat release (q') at a particular convection time delay, τ. Physically, τ is the time for the fuel to convect from injection to the flame. The $n-\tau$ Flame Transfer Function (FTF) is commonly used to model this relationship assuming an infinitesimally thin flame with a fixed τ. In practical systems, complex swirling flows, multiple fuel injections points, and recirculation zones create a distribution of τ, which can vary widely making a statistical description more representative. Furthermore, increased flame lengths and higher frequency instabilities with short acoustic wavelengths challenge the 'thin-flame' approximation.

The present study outlines a methodology of using distributed convective fuel time delays and heat release rates in a one-dimensional (1-D) linear stability model based on the transfer matrix approach. CFD analyses, with the Flamelet Generated Manifold (FGM) combustion model are performed and probability density functions (PDFs) of the convective time delay and local heat release rates are extracted. These are then used as inputs to the 1-D Thermoacoustic model. Results are compared with the experimental results, and the proposed methodology improves the accuracy of stability predictions of 1-D Thermoacoustic modeling.

Thermoacoustic Analysis and Experimental Validation of a Statistically-Based Flame Transfer Function Extracted from Computational Fluid Dynamics

Shrihari Sampathkumar

GENERAL ABSTRACT

Gas turbines that operate with lean, premixed air-fuel mixtures are highly efficient and produce significantly lesser emission of pollutants. However, they are highly susceptible to self-induced thermoacoustic oscillations which can excite larger pressure fluctuation which can damage critical components or catastrophic engine failure. Such a combustion system is considered to be unstable since the oscillation amplitude increases with time. Understanding the non-linear feedback mechanisms driving the system unstable and their cause are naturally of high interest to the industry.

Highly resolved, but computationally demanding simulations can predict the stability of the system accurately, but become bottlenecks delaying iterative design improvements. Low order numerical models counter this with quick solutions but use simplified representations of the flame and feedback mechanisms, resulting in unreliable stability predictions. The current study bridges the gap between these methods by modifying the numerical model, allowing it to incorporate a better representation of fluid flow fields and flame structures that are obtained through computationally cheaper simulations. Experiments are conducted to verify the predictions and a technique that can be used to identify regions of the flame that contribute to amplitude growth is introduced. The

improved model shows notable improvement in its prediction capabilities compared to existing models.

ACKNOWLEDGEMENTS

I wish to express my deepest gratitude to my research advisor, Dr. Joseph Meadows for giving me the opportunity to work on this thesis topic. In addition to fostering a truly well-rounded growth of my technical skills, his guidance and supervision helped mold all aspects of my professional life. I would also like to thank members of my committee, Dr. Burdisso and Dr. Tafti, for their guidance and support throughout the graduate program.

I thank the Mechanical Engineering Department for the Teaching Assistantship opportunity, an enjoyable learning experience. I specially thank Dr. Behkam and Dr. Rice for being understanding and flexible, making my duties much easier to manage.

I sincerely thank every member of my research group for their help, and for maintaining a friendly atmosphere in the lab. I would especially like to thank Cody Dowd for his guidance during every important stage of my thesis work, and Steven Wong in helping set up the instrumentation for the experimental rig. I am also grateful to the quality work of the ME Machine Shop and Randall Monk in fabricating parts for the setup. I would also like to thank the Advanced Propulsion and Power Laboratory (APPL) for providing the necessary testing facilities.

Enduring the past two years would not have been possible without all the fun and goofy moments, thanks to Sathya, Chidambaram, Sachin, Ashwanth, Hari Shankar and Sanjay. Sincere thanks to Vadivel, Goundamani, Ilayaraja, and Rahman for all the moral support through the years.

Last but certainly not the least, I would like to thank my family for their support, encouragement and love. Dad, thanks for all the sacrifices you have made to help me keep pursuing my dreams. Thank you Mom, Shruti and Grandma. I hope I can make all of you proud one day.

Table of Contents

Table of Figures

CHAPTER 1:

Thermoacoustic Analysis and Experimental Validation of a Statistically-Based Flame Transfer Function Extracted from Computational Fluid Dynamics

Shrihari Sampathkumar[1], Joseph Meadows[2]
Department of Mechanical Engineering, Virginia Tech, Blacksburg, 24060, USA

Submitted to ASME Journal of Gas Turbines and Power

Abstract

Lean premixed combustion has the advantage of reduced NO_x emissions, but is susceptible to thermoacoustic instabilities. These instabilities arise and sustain due to the coupling of unsteady heat release from the flame and the acoustic field. One potential driving mechanism for these instabilities arise when velocity fluctuations (u') at the fuel injection location causes perturbations in the local equivalence ratio and is convected to the flame location generating an unsteady heat release (q') at a particular convection time delay, τ. Physically, τ is the time for the fuel to convect from injection to the flame. The $n-\tau$ Flame Transfer Function (FTF) is commonly used to model this relationship assuming an infinitesimally thin flame with a fixed τ. In practical systems, complex swirling flows, multiple fuel injections points, and recirculation zones create a distribution of τ, which can vary widely making a statistical description more representative. Furthermore, increased flame lengths and higher frequency instabilities with short acoustic wavelengths challenge the 'thin-flame' approximation.

The present study outlines a methodology of using distributed convective fuel time delays and heat release rates in a one-dimensional (1-D) linear stability model based on the

transfer matrix approach. CFD analyses, with the Flamelet Generated Manifold (FGM) combustion model are performed and probability density functions (PDFs) of the convective time delay and local heat release rates are extracted. These are then used as inputs to the 1-D Thermoacoustic model. Experiments are performed with varying convective time delays by controlling flow velocities. Results from the 1-D thermo-acoustic model obtained, are compared with the experimental results. The proposed methodology improves the accuracy of stability predictions for 1-D Thermoacoustic modeling with a statistical n-τ FTF.

Nomenclature

a	Speed of sound
A	Amplitude of perturbation
c	Reaction progress variable
f	Frequency(Hz)
FTF	Flame Transfer Function
FWHM	Full Width at Half Maximum
G	Growth rate
GT	Gas Turbine
h	Enthalpy
j	Duct number

k	Wave number
LPM	Lean Pre Mixed
m	Mass flow rate
n	Interaction index
p	Pressure
Q / q	Heat release due to combustion
R.I	Rayleigh Index
T	Transfer matrix
Z	Mixture fraction
ϵ	Source term
ϕ	Equivalence ratio
μ	Mean
ω	Complex frequency
γ	Ratio of specific heats
ρ	Density
σ	Standard deviation

Subscripts

a	of air
eq	at equilibrium

f	of fuel
x	of flame location
τ	of time delay
ω	Complex
0	Mean

Superscripts

‘	Perturbation / unsteady term
f	of formation
+	Forward travelling wave
-	Reverse travelling wave

Introduction

Lean premixed combustion in Gas Turbines has the advantage of reduced NO_x emissions due to reduced flame temperatures; but is more susceptible to Thermoacoustic instabilities [1]. These instabilities generate high pressure amplitudes and can contribute to vibration induced wear and sometimes failure of critical components like fuel nozzles, combustor liners and transition pieces. This adversely impacts continuous operation by requiring downtime for repairs, inspections and sometimes replacement of damaged components [2].

Acoustic perturbations of pressure and velocity are amplified when the pressure fluctuations are in phase with the heat release rate fluctuations, and according to the Rayleigh criterion [3], instabilities grow when the energy added to the acoustic field by unsteady heat release exceeds the energy lost due to acoustic damping and viscous dissipation in the system. The growth rate of the pressure amplitude depends on its relative phase with unsteady heat release rates. Maximum amplitude growth occurs when heat addition is perfectly in-phase with the acoustic pressure and maximum damping results when they are perfectly out of phase [4, 5].

For the instabilities to be self-excited, a feedback mechanism becomes essential to transfer energy between heat release rates and the acoustic field. Fig 1 gives an overview of potential mechanisms in a typical combustion system. Z represents the impedance between the various components.

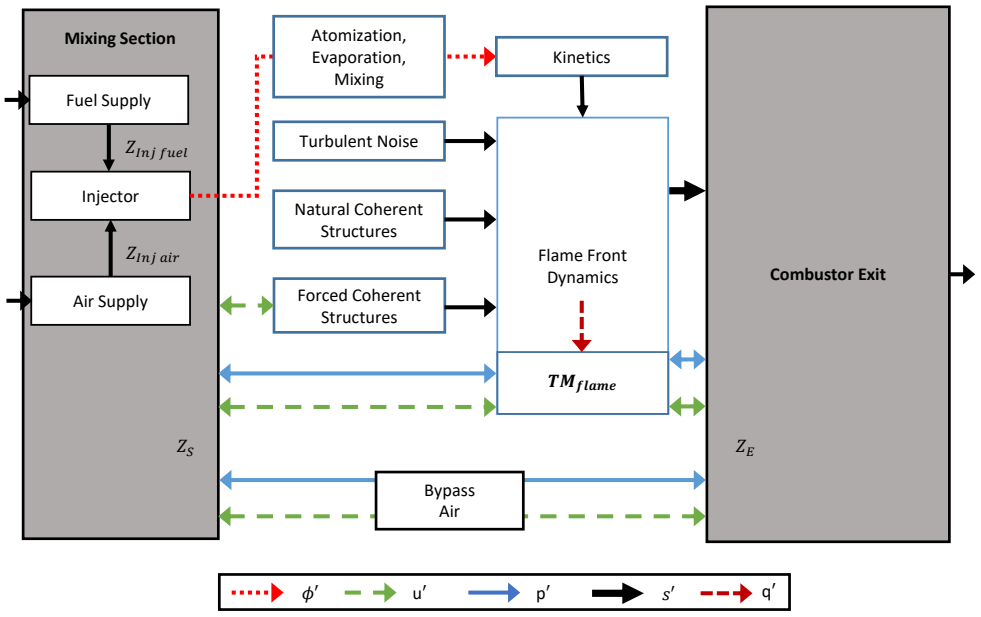

Fig 1: Mechanisms driving combustion instabilities

Acoustic pressure and velocity perturbations (p', u') produced at the flame front propagate both upstream and downstream through the entire combustor domain and are partially reflected at locations with a change in acoustic impedance. Sections of the combustor where fuel injection and mixing with air occurs are also affected by these perturbations [6]. Such disturbances in the fuel mixing section may lead to fluctuations of the equivalence ratio (ϕ'). The ϕ' perturbation is then convected to the flame and it directly influences the instantaneous heat release rate and temperature of the flame [7]. Perturbations at the mixing tube may also form flow structures at resonant frequencies and affect the heat release by changing the burning rate or skewing the flame surface (i.e. vortex-flame interactions) [8].

Understanding these mechanisms are important to determine and predict the system's thermoacoustic stability. Numerical and analytical tools are generally employed early in the design stage to make stability predictions. Large Eddy Simulations (LES) have

proven their prediction capabilities by simulating a computational 'twin' of the system [9-12]. However, these simulations are computationally expensive, making them a bottleneck during design. Conversely, low order analytical models provide quick solutions and hence have found a wide application in the industry [13-15].

Linear flame response models attempt to identify the stability of a system and their corresponding acoustic amplitude growth rates, while non-linear tools are used to predict the limit cycle amplitudes [16, 17]. In linear stability analysis, the flame transfer function (FTF) describes the coupling between heat release (q') and acoustic perturbations (p' and u') [15, 18]. The u' n-τ FTF is commonly used to describe the mechanism formed between q' and ϕ'. u' at fuel injection produces ϕ' which arrives at the flame after a convective time delay τ. This time delay determines the phase relationship between u' and q', dictating the nature of the feedback loop at a given instability frequency. A simplified representation of the flame is introduced through a thin flame approximation, which assumes an infinitesimal flame thickness. In practical systems, these approximations only hold true if the acoustic wave length is much larger than the flame thickness. Presence of recirculation zones, swirling flows and multiple injection locations add complexity to the system by introducing a distribution in the fuel time delay from injection to the flame. Similarly, axially elongated flames or presence of higher frequency instabilities bring acoustic wavelengths and flame thickness to a comparable order, making the thin flame approximation invalid [19].

The importance of the effect of convective time delays on stability modeling has been highlighted in multiple investigations [20-22]. In particular, Mongia et al. [22] have observed that for a frequency of 500 Hz the time delay range covers both positive and negative Rayleigh Index values. The study acknowledges that a single τ model needs to be

expanded to reproduce observed experimental behavior. In attempts to expand the complexity of the n-τ model, Kim et al. [5, 19] proposed a local heat release model for an experimental flame transfer function. The local flame transfer function was able to make better predictions when the flame thickness was greater than 10% of the acoustic wavelength. Similarly, the flame shape can have an effect on the predicted instabilities [23].

Studies that investigated the spread of the fuel time delay also prove that using a distributed τ on the instability predictions can significantly shift the stability map. Sattelmeyer [24] approximated a triangular distribution of residence times, based on the radial velocity distribution formed at the end of the fuel supply region. Armitage et al. [25] introduced a model that uses a uniform spread of time delay, which conform with experimental results better than the standard n-τ formulation. Similarly, the effect of both triangular distribution and Gaussian distributions of the fuel time delay were studied by Polifke et al. [26] and similar conformity between the proposed model and experimental results were shown. Existing studies have investigated the effect of distributed heat release on instabilities through experimental methods, and the spread of fuel time delay has been modelled in the FTF using simple distributions. However, n-τ FTF formulations that are capable of incorporating realistic, combined distribution of both spatial heat release and τ are non-existent.

In the present study, an improved version of the n-τ flame transfer function is developed by using statistical distributions extracted from CFD simulations. Predictions of instabilities and growth rates from the new statistical FTF deviate significantly from the n-τ FTF predictions. Experiments are conducted to validate the improved model and the

results prove that a combined distribution of the flame location and τ provide a much more accurate prediction of instabilities compared to previously used simplified models.

Theory and Methodology

Transfer Matrix Approach

The linear stability analysis technique is used to predict the growth or decay of acoustic oscillations with time. The numerical model uses a transfer matrix approach which solves a series of equations with acoustic pressure and velocity to determine the eigenfrequencies of the system. A realistic representation of a system can be constructed by considering a series of connected ducts with constant cross-sectional areas (Fig 2). Interaction of the flame with acoustics is described by a FTF. Therefore, the choice of FTF becomes a critical factor in the prediction of instabilities. The derivation for the equations used in the classical Transfer Matrix approach follows [18].

The equations governing acoustic velocity and pressure in 1-D are expressed as:

$$\frac{\partial u'}{\partial t} + \frac{1}{\rho_0}\frac{\partial p'}{\partial x} = 0 \tag{1}$$

$$\frac{1}{\gamma p_0}\frac{\partial p'}{\partial t} + \frac{1}{S}\frac{\partial (Su')}{\partial x} = \frac{\gamma - 1}{\gamma p_0}\, q' \tag{2}$$

Where S is the cross sectional area and q' is the unsteady heat release term. By assuming constant cross sectional areas and harmonic waves, the solution to the equations for the acoustic pressure and velocity are as follows:

$$p'(x,t) = A^{+}e^{i(kx-\omega t)} + A^{-}e^{i(-kx-\omega t)} \tag{3}$$

$$u'(x,t) = \frac{1}{\rho_0 c_0}\left(A^{+}e^{i(kx-\omega t)} - A^{-}e^{i(-kx-\omega t)}\right) \tag{4}$$

A^{+} and A^{-} are the amplitudes of the forward and backward travelling waves respectively, k is the wave number and ω the complex frequency. ρ_0 and c_0 are the density and velocity of sound at mean conditions. In the transfer matrix approach, the conservation equations are integrated across the interfaces in a series of ducts to get the jump conditions.

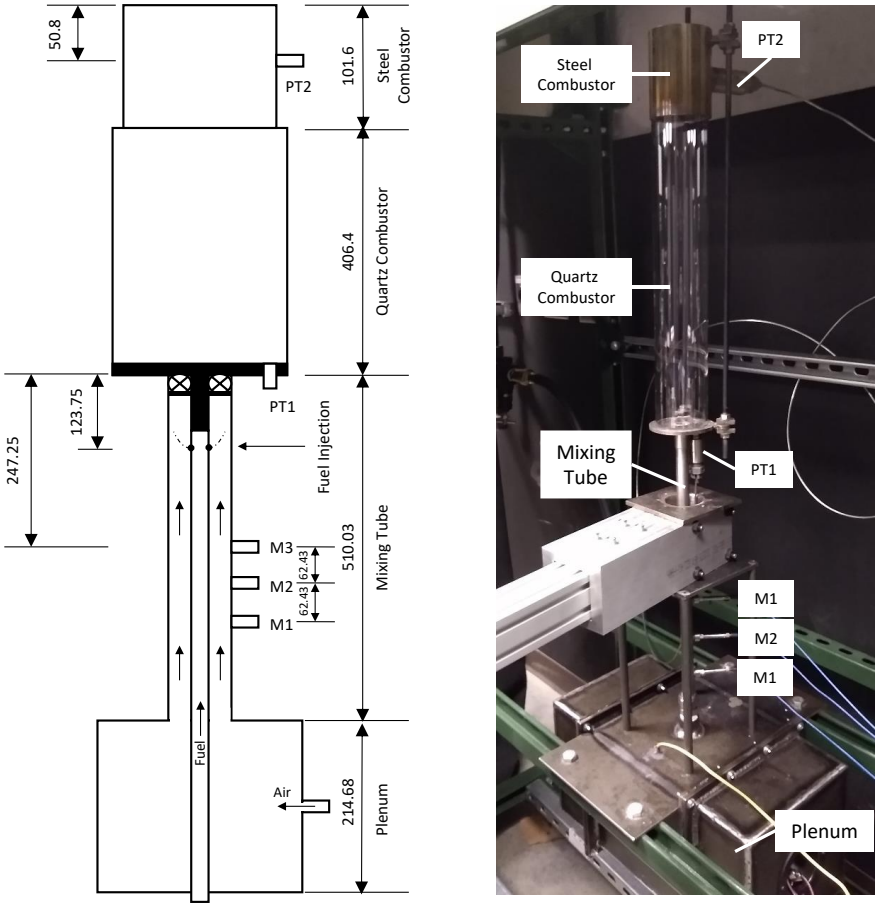

Fig 2: Schematic and Picture of Experimental setup (All dimensions in mm)

The amplitudes of waves in each of these ducts are related though the transfer matrix. Since the flame is assumed to be infinitesimally thin, it is included into the transfer matrix at an interface between two ducts. The jump conditions across the interfaces are obtained by integrating both sides as shown:

$$[p']_{x_{j+1}^-}^{x_{j+1}^+} = 0 \tag{5}$$

$$[Su']_{x_{j+1}^-}^{x_{j+1}^+} = \frac{\gamma-1}{\gamma p_0}\dot{\Omega}_T' \tag{6}$$

Where $\dot{\Omega}'_T = \int_{x_{j+1}^-}^{x_{j+1}^+} S\, q' dx$ is the total unsteady heat release produced by the flame, and

$$\int_{x_{j+1}^-}^{x_{j+1}^+} S q'\left(x_{flame}, t\right) dx = \frac{S_j \cdot n}{\gamma - 1}\, u'\left(x_{flame}, t - \tau\right) \tag{7}$$

Here j represents the duct number and x_{j+1} stands for the axial coordinate of the interface between ducts j and j+1. Superscripts + and – indicate the right and left of the interface, respectively. The system of equations for a series of ducts with a flame can now be assembled as a global transfer matrix as shown in (eqn 8-12):

$$\begin{pmatrix} A_{j+1}^+ \\ A_{j-1}^- \end{pmatrix} = G_{j,1} \begin{pmatrix} A_1^+ \\ A_1^- \end{pmatrix} + \Sigma_{k=1}^{J-1} G_{j,k+1} O_k + O_j \tag{8}$$

Where the global and local transfer matrices can be defined as:

$$G_{j,n} = T_j \ldots T_{n+1} \cdot T_n \tag{9}$$

$$T_j = \frac{1}{2} \begin{bmatrix} e^{ikl_j}\left(1 + \Gamma_j\right) & e^{-ikl_j}\left(1 - \Gamma_j\right) \\ e^{ikl_j}\left(1 - \Gamma_j\right) & e^{-ikl_j}\left(1 + \Gamma_j\right) \end{bmatrix} \tag{10}$$

Γ_j is called the section factor, defined as:

$$\Gamma_j = \frac{\rho_{j+1} c_{j+1}}{\rho_j c_j} \frac{S_j}{S_{j+1}} \tag{11}$$

The O_j matrix is a source term that applies the n-τ FTF:

$$O_j = \frac{1}{2} \frac{\rho_{j+1} c_{j+1}}{S_{j+1}} \begin{pmatrix} \frac{\gamma - 1}{\rho_j c_j^2} \Omega \\ -\frac{\gamma - 1}{\rho_j c_j^2} \Omega \end{pmatrix} \tag{12}$$

Distributed Time Delay

The spread of fuel convective time delay can be represented statistically using probability density functions (PDF). The PDF of the distribution (f_τ), multiplied with the

standard n-τ formulation and integrated from $-\infty$ to ∞ gives a mean effect of the distributed τ on the heat release. This results in eqn. 11:

$$\frac{\gamma-1}{\rho_1 c_1^2}\dot{\Omega}_{\mathrm{T}}^1 = S_j n u_1(x) \times \int_{-\infty}^{\infty} e^{i\omega\tau}\, f_\tau(\tau).\, d\tau \tag{13}$$

The distributions extracted from numerical results may not follow a standard statistical distribution. For such cases, a numerical probability density function is used to accommodate the τ spread. A histogram of the τ variation can be used to generate a piecewise probability density function:

$$f_{\tau,m} = \begin{Bmatrix} p_1/w_1\,, \tau_0 < \tau < \tau_1 \\ p_2/w_2\ \ , \tau_1 < \tau < \tau_2 \\ . \\ . \\ p_m/w_m\ \ , \tau_{m-1} < \tau < \tau_m \end{Bmatrix} \tag{14}$$

Where $p_m = \frac{N_m}{N_{total}}$ is the probability of the bin. m is the bin index and $w_m = \tau_m - \tau_{m-1}$ is the bin width. τ_m and $\tau_{\mathrm{m-1}}$ are the upper and lower bounds of τ values in a given bin. The n-τ FTF with a numerical τ distribution therefore becomes:

$$\frac{\gamma-1}{\rho_1 c_1^2}\dot{\Omega}_T^1 = S_j n \left(\sum_{m=1}^{m_{max}} \int_{\tau_{m-1}}^{\tau_m} f_{\tau,m}\, .\ e^{i\omega\tau} d\tau\right) u_1(x) \tag{15}$$

Distributed Heat Release

Similarly, analytical models with a distributed flame have shown improved predictability when compared to experiments [19, 23].To include this distribution into the n-τ FTF method, a series of flames can be used to account for the spread in the axial direction. A local FTF is calculated for each flame in this series of flames and their contribution to the global FTF is proportional to the fraction of the total heat released by the local flame.

$$\frac{\gamma-1}{\rho_j c_j^2}\Omega' = S_j u'\left(x_{f\eta}, t-\tau\right) \cdot n \cdot \frac{\mathrm{Q_{local}}}{\mathrm{Q_{total}}} \quad (16)$$

Where $x_{f\eta}$ is the location of the η^{th} flame. Q_{local}/Q_{total} represents the fraction of heat released by a local flame to the total heat released in the combustion chamber. When multiplied by the global interaction index, it gives a weighted local interaction index that determines the contribution of the η^{th} local flame.

Combined Spatial Heat Release and Time Delays

To include both distributions, a series of flames are constructed. Each flame is considered to be a separate interface and the individual convective time delay distributions at each of those interfaces are found. The local FTF is computed by combining both the probability density functions as:

$$\frac{\gamma-1}{\rho_j c_j^2}\Omega' = S_j u'\left(x_{fn}\right) \cdot \mathrm{n} \cdot \frac{\mathrm{Q_{local}}}{\mathrm{Q_{total}}} \cdot \int_{-\infty}^{\infty} e^{i\omega\tau} f_{t,m}(\tau).\, d\tau \quad (17)$$

The distributed time delay, distributed heat release and the combined distributions are implemented in a 1-D numerical solver, similar to the one developed by Dowd and Meadows [27], which has been verified with theoretical, canonical cases where analytical results are available.

Mass Entrainment Effect on Open Boundaries

The extreme boundaries of the combustor are taken as a rigid wall at the plenum end ($u' = 0$) and a pressure release at the combustor end ($p' = 0$). In these idealized cases, the reflection coefficient ($R = A^-/A^+$) is a real number, 1 and -1 respectively. However, for real problems, the boundaries behave in a more complex manner that can be modelled as a mass/spring/damper system, resulting in complex impedances and reflection coefficients (Fig 3).

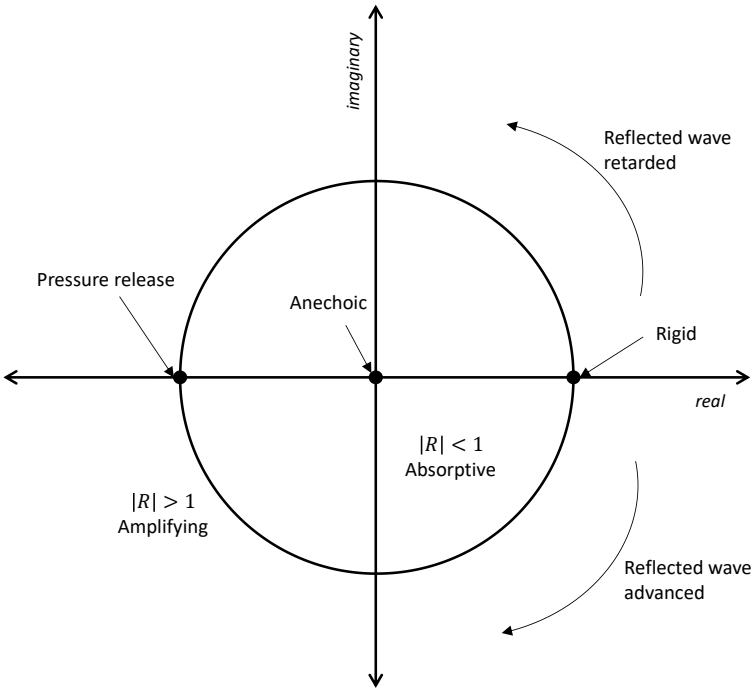

Fig 3: Polar plot of complex reflection coefficient, R

At the combustion chamber exit, the waves induce kinetic energy on the flow near the boundaries, which is analogous to adding an 'entrained mass' at the exit, making R complex. An additional 'entrainment length' ($L_{entr} = 0.6 \times radius_{duct}$) is added at the exit as a simple way to account for the phase shift introduced due to this effect [28].

Extraction of Numerical Flame Transfer Functions (Computational Methods)

The combustion system with the separate fuel and air streams is modelled in CFD. Turbulence is modelled using the k-Ω model. The segregated fluid enthalpy model is used with a 2-nd order accuracy convection scheme. Gradients are calculated using the Hybrid Gauss – Least Squares method with second order accuracy. The Flamelet Generated Manifold (FGM) model is used to model combustion. The model uses the GRI 3.0 mechanism to generate flamelets in reaction progress space and mixture fraction space. This method conserves computational resources by transporting mixture fraction (Z) and

reaction progress variable (c), while species mass fractions, temperature, and combustion source terms are tabulated a priori as a function of reaction progress and mixture fraction. The reaction progress variable is defined as:

$$c = \frac{X_{CO}+X_{CO_2}}{X_{CO,eq}+X_{CO_2,eq}} \tag{16}$$

Where X is the mass fraction of the species and the subscript eq indicates mass fractions taken at equilibrium. The model assumes all the combustion to take place in regions between unburned reactants (c=0) and completely reacted products (c=1). The FGM Kinetic Rate model is used for turbulence closure, since the results are insensitive to the type of model used [29]. The mesh consists of approximately 600,000 polyhedral cells.

Local volumetric heat release rate in a computational cell is computed with the net production rate of species and their corresponding enthalpies of formation:

$$Q_{local} = \Sigma_{\mathrm{i}}\left(\epsilon_i \cdot h_{0,i}^{f}\right) \tag{17}$$

ϵ_i is the source term accounting for the formation or destruction of chemical species, and $h_{0,i}^{f}$ the enthalpy of formation of the i^{th} species. The region closest to the dump plane with notable heat release is axially divided into multiple sections and the total heat release in each section is the sum of local heat release rates of all the cells within.

The Lagrangian Multiphase Particle Tracking model is used to extract the fuel convection time (τ) distribution from the plane of injection to the flame front. Each cell surface at the fuel injection boundary serves as an injector of massless particles, which are tracked. 2300 such particles spread among 6 fuel injection inlet holes (Fig 4) are introduced into the domain. Each particle records variables (including particle residence time and reaction progress variable) in every cell it travels through the domain from the injector to

outlet. τ values are obtained by defining the flame at a reaction progress variable value of 0.5 and a histogram of τ distribution is generated (Fig 5).

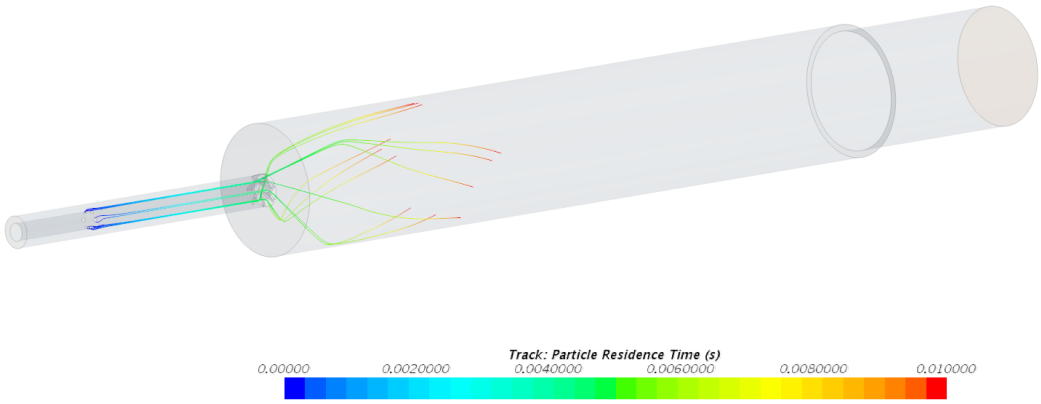

Fig 4: Particle Tracks of 20 arbitrarily selected particles injected into the combustor domain through 6 fuel injection holes.

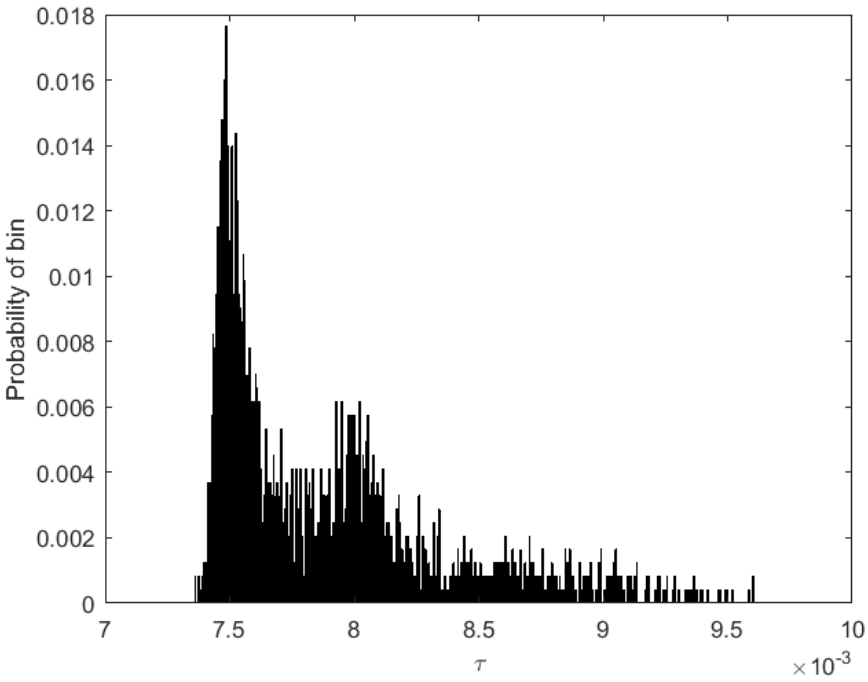

Fig 5: Histogram of fuel time delay at flame front extracted from CFD

To use the combined spatial heat release and time delay distributions, the single flame would be divided into multiple local flames. Fig 6 (A&B) shows a histogram of particles that reach the flame (c = 0.5), and the mass flow averaged heat release in the axial direction, respectively. When the flame is divided into sections, a histogram of τ values similar to Fig 5 is computed in each of these sections.

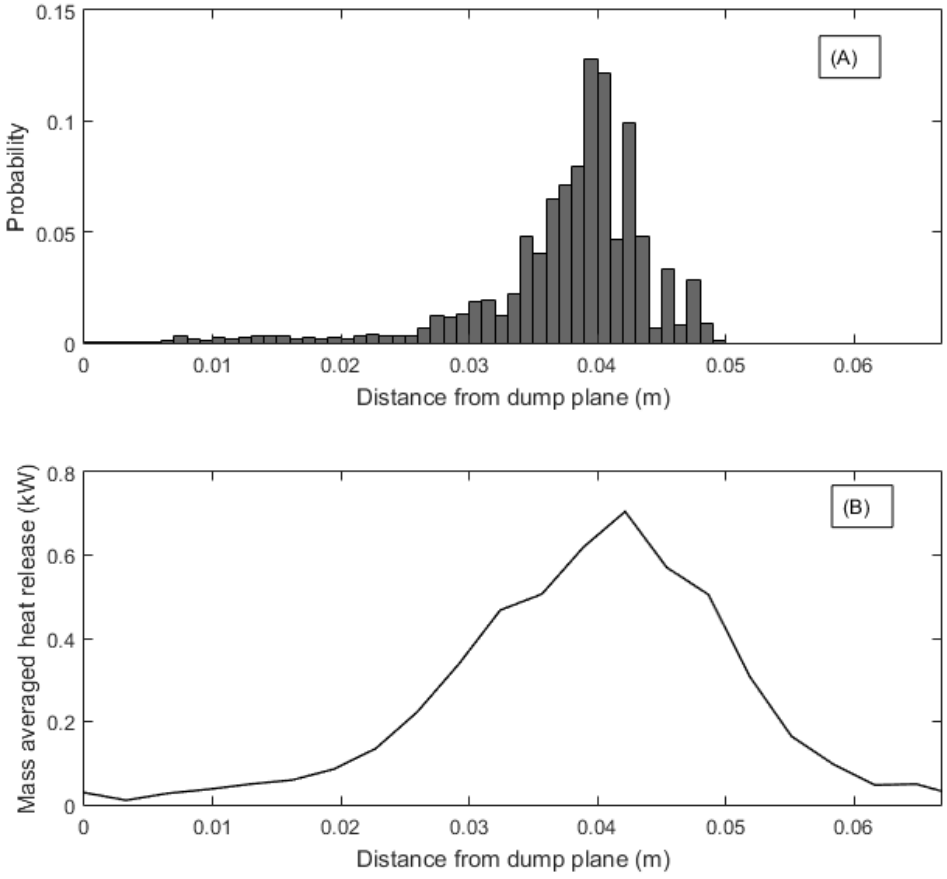

Fig 6: (A) Histogram of the probability of fuel particles reaching the flame front at an axial distance from the dump plane. (B) Mass Flow Averaged heat release as a function of axial distance from dump plane

Experimental Method

Experimental Setup

The experimental measurements are performed in a lean, partially premixed, swirl stabilized combustor, schematically shown in Fig 2(A). The combustor consists of a plenum, an annular mixing section, an optically accessible quartz-glass combustion section and a steel combustion section. Air is injected into the plenum through a choking plate to ensure a well-defined acoustic boundary condition. Mass flow controllers (Alicat MCR) are used to modulate the rates of air and fuel(methane) injection into the system. Air flow can be controlled up to flow rates of 10.34 g/s (500 SLPM) and the fuel up to 0.546 g/s. A $\pm$0.8% uncertainty of the reading is expected in these controllers, which translates to a maximum uncertainty of 82.6 mg/s and 4.37 mg/s (4 SLPM and 0.4 SLPM) in the air and fuel controllers respectively. The mixing tube is a 0.510 m annular tube with an outer diameter of 17.145 mm (0.675”). Fuel is delivered 123.75 mm upstream the base plate via a fuel rod, centered in the mixing tube with a 9.525 mm (0.375”) outer diameter, and is injected through 6 injection holes with equiangular spacing.

A jet-and-crossflow mechanism is used to inject the fuel into the air stream and allowed to mix. A 45° flat vane axial swirler, producing a swirl number 0.6, is flush mounted with the base plate at the end of the mixing tube. The combustor consists of a quartz section (inner diameter = 70 mm; length 190.5 mm) followed by a stainless steel section (inner diameter = 64 mm; length = 101.6 mm).

Instrumentation

Pressure perturbations are measured using an array of microphones (PCB ¼” ICP Microphone system) in the mixing tube and dynamic pressure transducers (Kistler 6025A)

in the combustion chamber. The microphones have a sensitivity of 2 mV/Pa, capable of sampling data at 4 Hz – 80kHz. The dynamic pressure transducers have a sensitivity of 103 pC/bar and a maximum rated operating temperature of 700˚C. Signal from the dynamic pressure transducers is amplified by charge amplifiers with a 200 mV/pC gain. The microphones and pressure transducers are synchronously sampled at a frequency of 100 kHz. The microphones (labeled M1-M3 in Fig 2 are equally spaced with a 62.43 mm pitch and the microphone closest to the base plate is placed 247.25 mm from it. One pressure transducer (PT1) is mounted to the base plate and the other pressure transducer (PT2) is mounted 50.8 mm (2 in) from the exhaust of the combustor.

A high speed intensifier (Specialized Imaging SIL1200-01-H03) and high speed camera setup (Photron FASTCAM SA5), with a monochromatic filter (310 nm FWHM 10 nm) points at the base plate region of the combustion chamber's quartz section and is used to capture the OH* chemiluminescence emission intensity from the flame. The chemiluminescence images are used to quantify the heat release response. The images are captured at 3000 Hz with a 1024 x 1024-pixel resolution. The spatial resolution of the images obtained are 6.62 pixels/mm. The camera, microphones and pressure transducers are set up to achieve synchronized data acquisition. All tests were performed at atmospheric pressure in the combustor with inlet air and fuel at room temperature.

Results and Discussions

Experimental

Characterization of self-excited instabilities is necessary in order to create a stability map of the combustion system. Convective fuel time delay, being one of the primary variables considered in this study is controlled by testing a range of air flow rates from 1.03 g/s (50 SLPM) to 10.34 g/s (500 SLPM) with a 0.206 g/s (10 SLPM) spacing. A constant equivalence ratio is maintained at 0.85 for all flow rates. For the n-τ solver, the location of the flame is defined at the axial location where maximum heat release occurs in CFD. The convection time delay estimated in the experimental cases is calculated based on the distance between fuel injection and the flame location, and using bulk velocity of the gaseous mixture. Pressure and heat release measurements are recorded after the system reaches steady state.

Based on the coupling between the overall heat release and pressure fluctuations explained in the proceeding sections, 137 dB (141.5 Pa) is chosen as the lower limit that defines an unstable system. By this definition of instability, the system is characterized to be unstable between fuel time delays of 18 ms and 6.5 ms (Fig 6). At τ values close to these limits, which are considered to be the transition regions, a higher uncertainty in the Sound Pressure Levels (SPLs) is observed when compared to either the stable or unstable operating conditions. Similar to the uncertainties in SPL, a high level of uncertainty in the frequencies of instabilities are seen near the transition regions as well. In the stable cases, the peaks in the Fourier spectra (Fig 8) correspond to the natural frequencies of the system which are mildly excited to amplitudes that are still several order of magnitudes lower than unstable cases. In the unstable region, the excited frequencies fluctuate within the 300 Hz

to 350 Hz range. As the flow rates are increased, heat addition rates to the system increase at a faster rate than the heat loss, increasing the average duct temperature. Elevated duct temperatures drive the excited frequencies higher at these lower τ values.

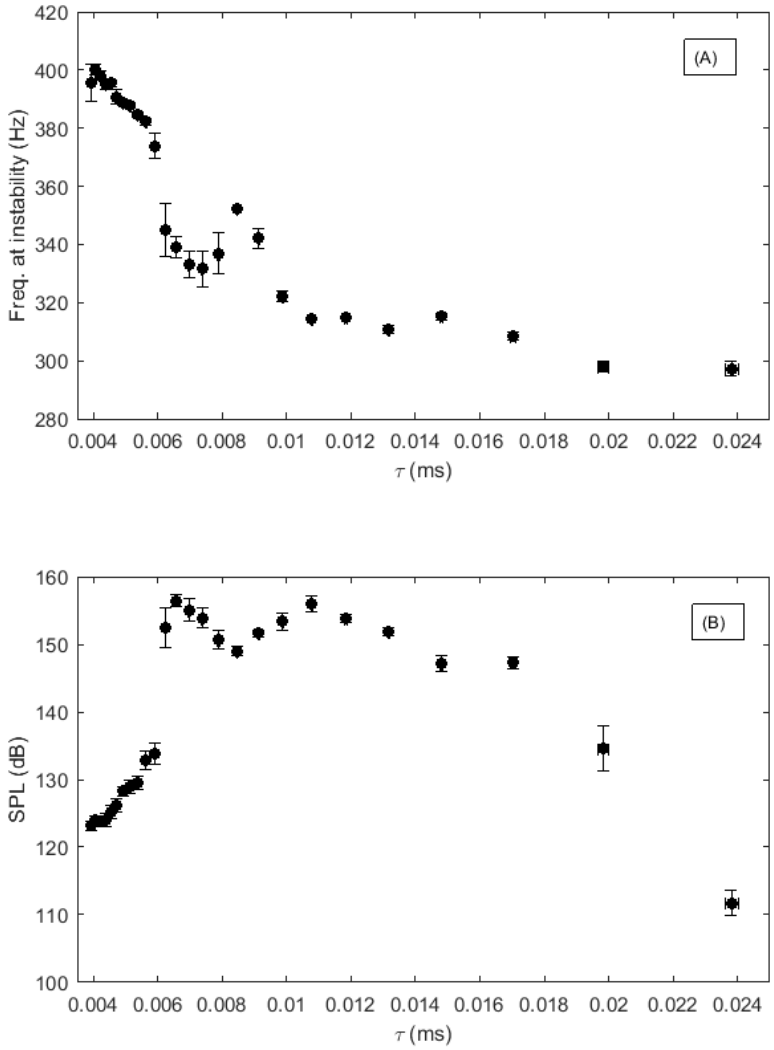

Fig 7: (A) The maximum pressure oscillation amplitude for τ values in the mixing tube (microphone M1). (B) The frequency at the maximum pressure fluctuation amplitude

Fig 8 shows the typical Fourier spectra of microphone data from the mixing tube in stable and unstable cases. The peak pressure amplitude in the unstable case is multiple orders of amplitudes greater than the stable case. The higher harmonics of the base

instability frequency are observed for the unstable case. In the stable case, these higher harmonics are either not excited or are below the noise floor of the microphone.

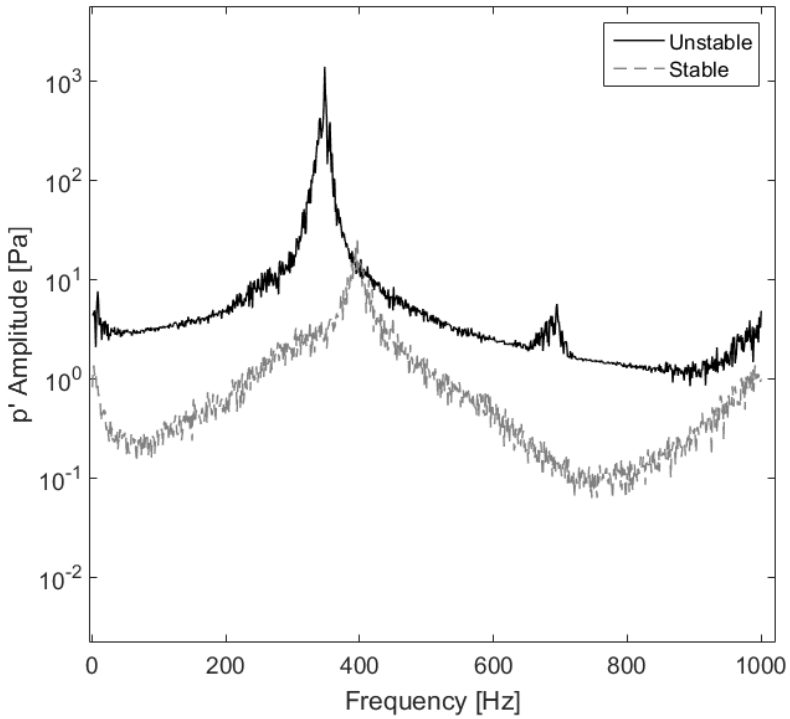

Fig 8: Spectra of pressure amplitudes recorded by microphone in the mixing tube (M1) for unstable (τ = 4.56 ms) and stable (τ = 3.68 ms) conditions

The time traces of the sum of normalized OH* chemiluminescence intensities and pressure recorded at the dump plane (Fig 9) show the positive phase relationship between the fluctuations in heat release rates and the acoustic pressure for the unstable case. From the Fourier analysis (Fig 10), the frequency of the heat release fluctuation is within ± 2 Hz of the frequency of the instability. Also, the OH* chemiluminescence images clearly capture the higher harmonics of the base instability.

In stable cases, even if a peak is visible in the pressure spectrum (Fig 8), the amplitudes of the corresponding q' fluctuation are much closer to the noise floor and no

clear coupling can be identified in the time signal. The existence of such a coupling between the heat release and pressure fluctuations also support the defined stable/unstable limit of 137dB.

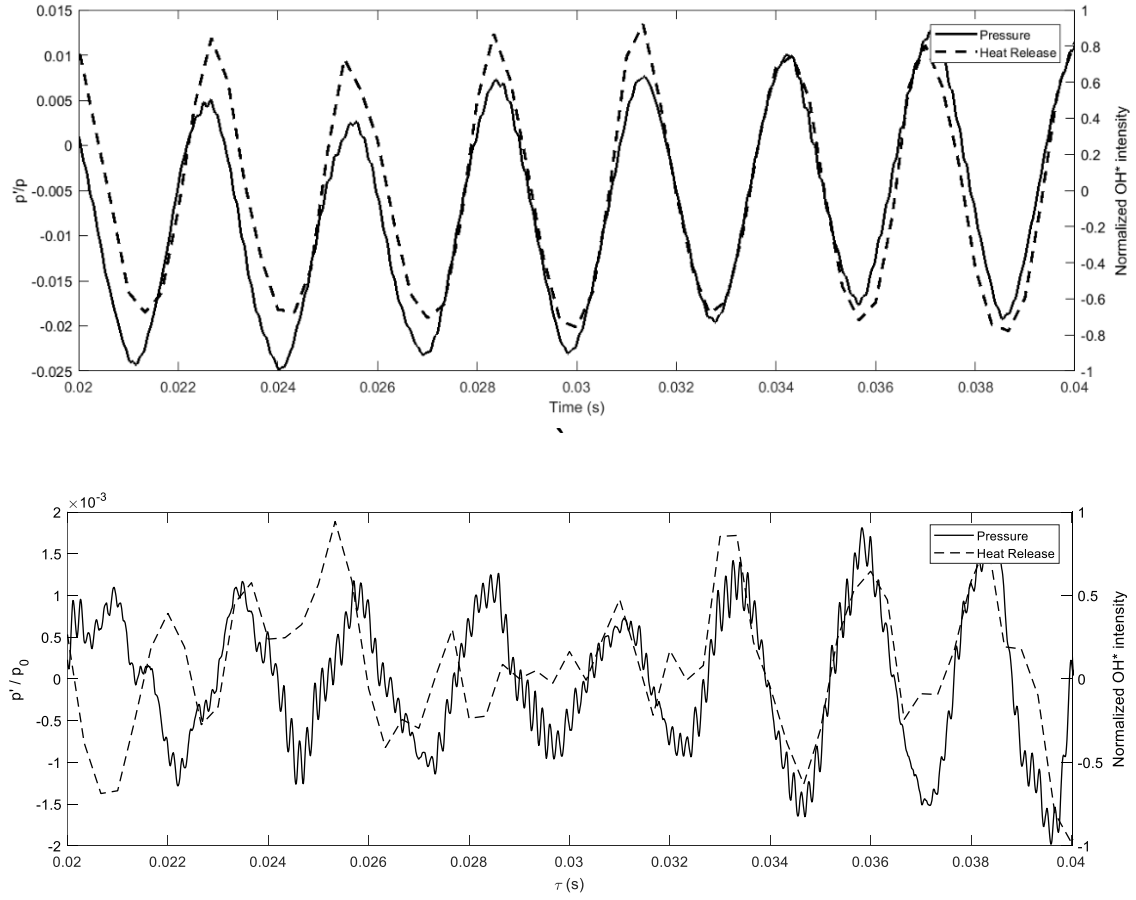

Fig 9: Time traces of normalized OH* intensity and relative pressure p'/p_0 for unstable (top) and stable (bottom) cases

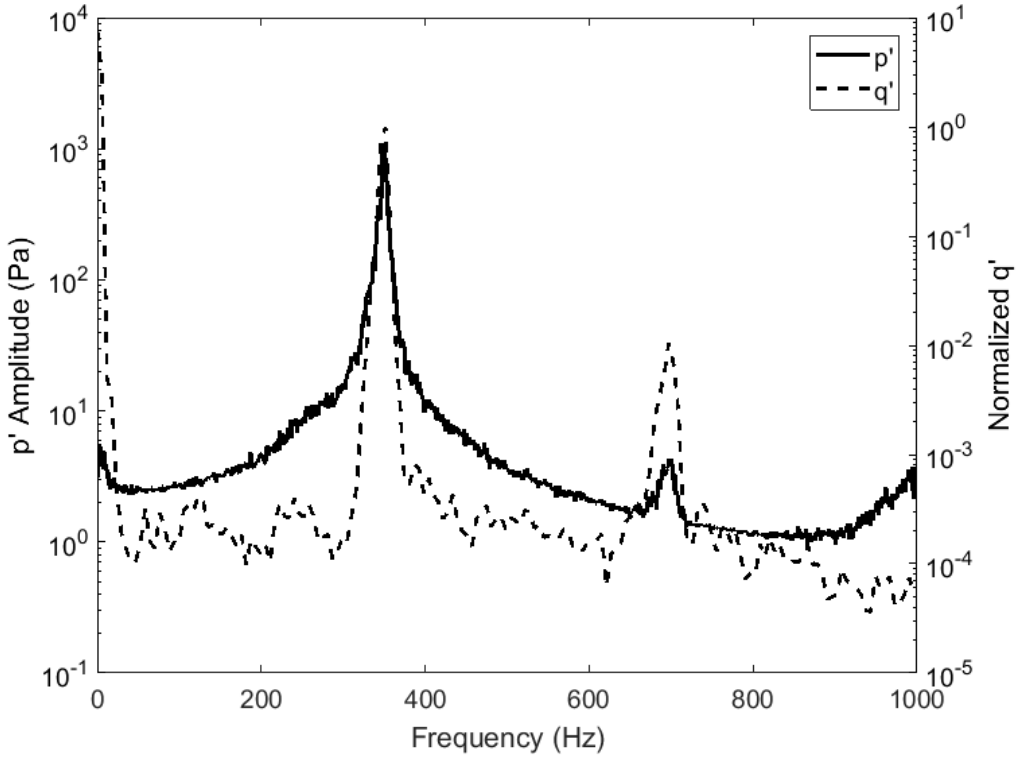

Fig 10: Spectra of pressure fluctuations and normalized q' values in an unstable case

Reconstruction of Pressure Mode Shapes

A key comparison that can be drawn between numerical models and experimental observations are through the acoustic mode shapes of the system. Recently, a technique used to reconstruct the pressure wave shapes from experiments using surface-mounted pressure transducers was developed by Hale et al. [30]. It is based on a least-squares curve fit method [31] and is capable of decomposing the components of mixed, non-stationary waves.

The reconstructed wave structures are used to evaluate the accuracy of the predicted mode shapes from the 1-D model. The location of pressure nodes and antinodes can be traced at each time step. The individual amplitude coefficients of the acoustic wave, namely

the forward and reverse travelling waves can also be distinguished. Boundary conditions and impedances can be indirectly verified through this method since it is an extension of the two-microphone method. Through the reconstructed waves, the pressure at a particular axial location can be approximated at a given time step. As an extension, this axial pressure data, combined with the OH* chemiluminescence images, provides the data required to calculate the local Rayleigh Index in the combustion region.

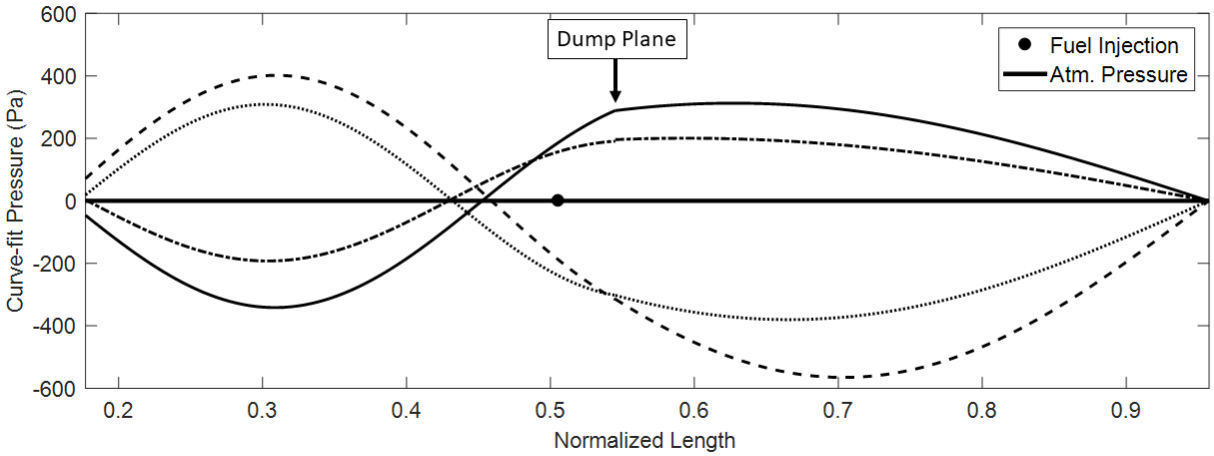

Fig 11: Reconstructed wave plotted at different phase angles. (Flow condition: τ = 6.8 ms).

Since pressure data is recorded in the mixing tube and combustion chamber sections, the wave reconstruction is performed only in these two regions. The boundary where the mixing tube opens into the plenum has a large area ratio and based on both experimental observations and from the model results, it can be approximated as an open boundary. However, a small pressure amplitude might still be present at this plane since it is not a perfectly open boundary. Allowing a $\pm 100\ Pa$ tolerance at this plane instead of using zero increases the goodness of fit (r^2 value) by 0.3 and keeps the overall r^2 value higher than 0.9. Pressure at the combustor exit is set to zero since it is an actual open boundary.

A cosine function (eqn 18) represents the resultant of two counter travelling pressure waves in a duct at a time sample.

$$p'(x,t) = C\cos(kx + \gamma) \tag{18}$$

$$C = \sqrt{A^{+2} + A^{-2} + 2A^{+}A^{-}cos(\phi)} \tag{19}$$

Where the amplitude coefficient C is the vector sum of the forward (A^{+}) and reverse (A^{-}) wave amplitude coefficients and ϕ is the phase angle between the waves. k is the wave number and γ is the least-squares curve-fit function phase angle. C is approximated from the maximum pressure value from the raw pressure data and k based on the frequency of instability and temperature in the respective ducts. C and γ are treated as unknowns in the curve fits, and temperature is estimated based on flame temperature calculations. In the present form, a continuous wave can be reconstructed in a duct where there are no changes in impedance or area change due to the simplicity of the function used for the curve fit. A minimum of two data points are necessary to solve for the unknowns C and γ while using an approximate k. Addition of a third data point eliminates the need for such approximations while capturing any mode switching that might occur in the duct.

Reconstruction of waves from the raw pressure data is possible only when the instabilities are sufficiently strong to differentiate it from noise and higher harmonics. Naturally, this procedure therefore becomes feasible only the cases defined to be unstable (6.5 ms< τ <18 ms) by the criteria stated above ($|p|$ > 137 dB). Fig 11 shows the reconstructed wave structure for an unstable case (τ = 6.8 ms). A full wave is predicted within the mixing tube and the combustion chamber, and the pressure node is close to the fuel injection point. Even though the frequency shifts over a range of 40 Hz in the unstable

region, the reconstructed wave shapes predict a similar full wave structure for all unstable cases.

The location of the pressure node is also seen to slightly shift during a complete cycle of the pressure oscillations, indicating that the system does not have a perfectly stationary wave. The axial location of pressure node, which corresponds to a velocity antinode, is close to the axial location of fuel injection located at a normalized length of 0.488 (Fig 11). This proximity suggests that the mechanism driven by equivalence ratio fluctuations are encouraged in this configuration.

Using the analysis outlined in [30], the amplitude coefficients of the forward and backward travelling waves can be identified in both ducts. Physically when the coefficient of one wave component is larger than the other, the reconstruction predicts a non-stationary wave, moving in the direction of the coefficient with the larger amplitude. The difference between the coefficients obtained through this analysis suggests a forward travelling wave for all the unstable cases. Mean flow effects, which lead to advection of the acoustic waves in the flow direction, are not insignificant in the swirler section where reactant velocities are accelerated through the restricted cross section. The advection effects introduce an $O(M)$ correction to the phase relation between the waves [32]. The Mach number, being relatively low at 0.2, in a section that measures 0.1 m in the axial direction only introduces a weak shift in the amplitude coefficients. In Fig 11, the axial location of the pressure node does not shift much during the entire pressure cycle, confirming that the effects of advection cause only slight deviations from the standing wave assumption (no mean flow) in the model.

The accuracy of the analysis method is also limited by the goodness of fit values in the least-squares curve fit method. A non-stationary wave can be suggested if the axial location of the pressure node moves at any time step. Therefore, only cases that have a significant difference between the coefficients can be reliably assumed to have a non-stationary wave.

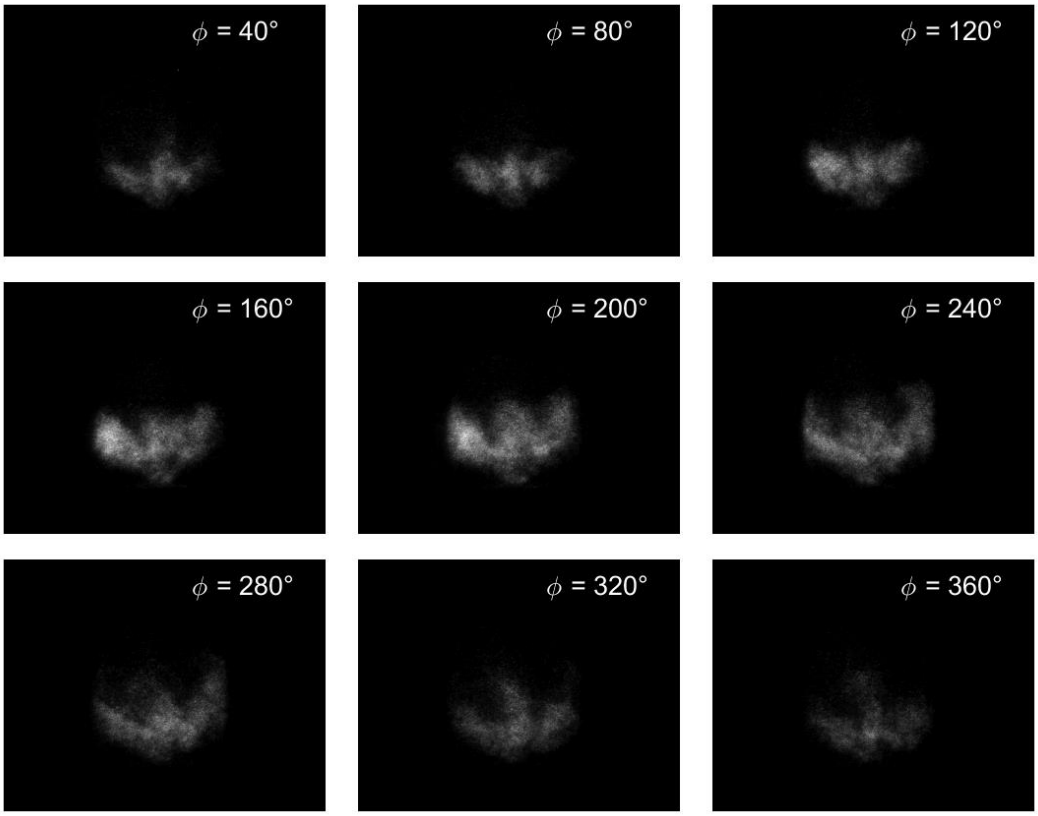

Fig 12: Phase synchronized OH* chemiluminescence intensities during a complete cycle of oscillation at an instability frequency of 350 Hz and τ delay of 6.8 ms

OH* Chemiluminescence and Rayleigh Index Images

The line-of-sight integrated OH* chemiluminescence intensity images (Fig 12) correspond to the spatial heat release rates of the flame. The direction of flow of the reactants is from the bottom to the top. The images obtained are in phase with the pressure cycle measured at the dump plane (PT1) at the frequency of instability (350 Hz). Peak heat

release is observed to occur around the 160-200° phase angles. To calculate the unsteady heat release rate fluctuations (q'), the average intensity of every pixel over a complete cycle is subtracted from the instantaneous values and are considered proportional to the heat release fluctuations (Q').

To obtain 2-D projection of spatially resolved Rayleigh Index images, data from the pressure wave reconstruction and the chemiluminescence images are combined. The spatial resolution of the chemiluminescence images are approximately 6.62 pixels/mm. The Rayleigh Index at each pixel is calculated by:

$$RI(x_p, y_p) = \frac{1}{T} \int_T q'(x_p, y_p, t) p'(x_p, y_p, t) dt \quad (19)$$

Where x_p and y_p are coordinates of the pixel. Interpolated images are first calculated so that a value of q' is available along with the p' value at each time step for integration. Numerical integration over a complete cycle in each pixel yields an image of the 2-D projection of spatially resolved Rayleigh Index (Fig 13 A,C). By definition, positive values contribute to the growth of pressure amplitudes and negative values have a damping effect. Since both wave reconstruction and chemiluminescence imaging can be performed at real time, spatially resolved Rayleigh Index can be calculated for every cycle of the oscillations. In the Rayleigh index images, the amplitudes of the indices computed are much higher for the unstable case, due to higher p' amplitudes.

A clear distinction between regions with positive and negative Rayleigh indices is made by grouping pixels based on their sign (Fig 13 B&D). Noise in the raw images contribute to error in the Rayleigh Index images and are hence filtered by setting their values to zero. The high fraction of pixels which have a positive Rayleigh Index (yellow) in the unstable case is highlighted through the tricolor images. In the stable case, only

regions close to the centerline has a positive Rayleigh Index and the other regions of the flame dampen the pressure amplitudes. The volume integrated Rayleigh Index values for the unstable and stable cases are 1.2016×10^9 and -4.2428×10^6 respectively, and their signs confirm the stability of these cases. Observations where the SPL is greater than 137 dB typically have a positive Rayleigh index while those below 137 dB have a negative value, confirming the threshold defined for instability.

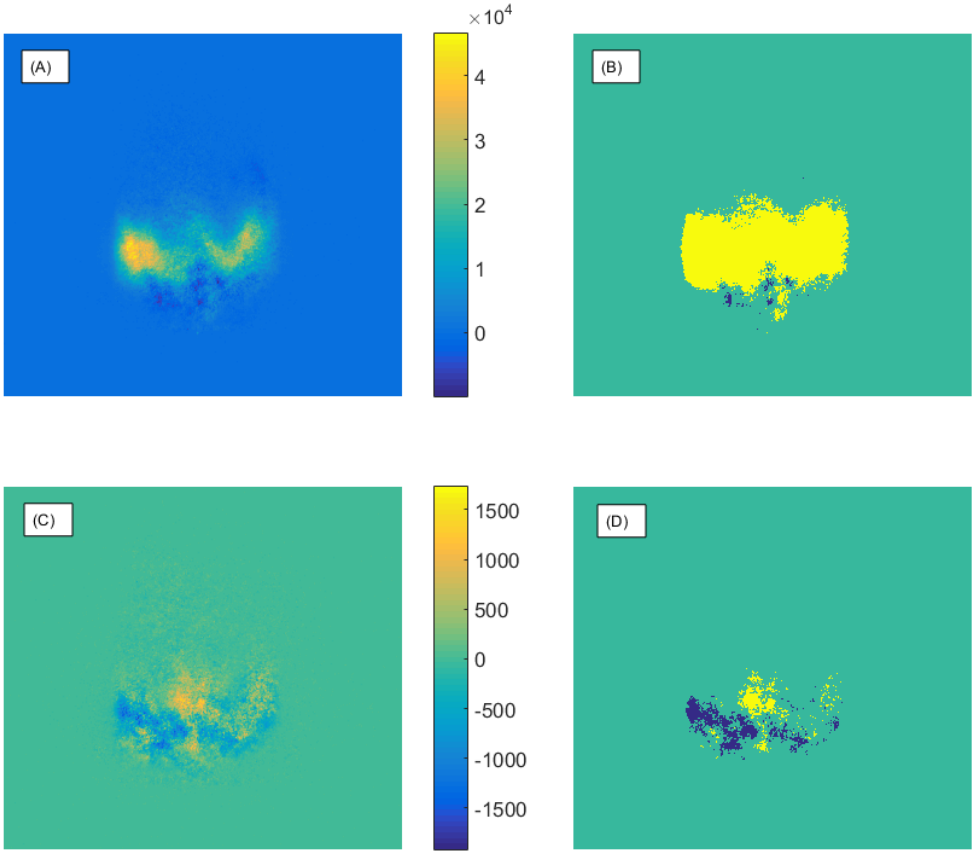

Fig 13: Rayleigh Index images for unstable (top) and stable (bottom) cases. (A, C): Rayleigh Index calculated over a complete cycle at each pixel. (B, D): Pixels with positive and negative Rayleigh Indices. (Yellow = positive, Blue = negative, Green = Noise/Zero)

1-D n-τ model results

For the normal n-τ solver predictions, the location of the thin flame is assumed to be the axial location with maximum heat release in the CFD simulations. For an equivalence ratio of 0.85 used in the experiments, the adiabatic flame temperature for a methane-air flame is 1919K. To determine the sensitivity of the solver to heat loss by the combustion products through the quartz and stainless steel sections of the combustion chamber, a temperature sweep for values below the adiabatic flame temperature is performed (Fig 14).

Frequencies and pressure mode shapes predicted by the solver are sensitive to the assumed combustion chamber temperature, since it directly influences the speed of sound. Generally, increasing the predicted temperature in the combustion chamber correspondingly increases the frequency (f) for a given mode. Since the strongest instabilities observed in the experiment mostly lie within the 300 Hz to 420 Hz range, the solutions from the solver that lie within or are closest to this range are used for comparisons. A 1700K temperature assumption in the combustion chamber predicts a full wave mode in the mixing tube and combustion chamber (Fig 15) for a frequency of 398.4 Hz. Lower temperatures, such as 1500K predict a half wave mode even though the frequency (379.3Hz) lies within the experimentally observed range. The wave mode reconstruction from experiments indicate a full wave in the system, favoring the 1700K temperature assumption. Although an arbitrary temperature assumption is being followed at present, better thermal modelling of the system in CFD will allow for a physics based temperature assumption.

The n-τ solver predicts a τ difference between peak growth rates to be close to $1/f$ (Fig 14) since ω in the $e^{i\omega\tau}$ term of the FTF formulation is inversely related to f. However, the range of τ over which the system is unstable in the experiments is nearly thrice that of the predicted instability range, suggesting that the unmodified n-τ FTF is not effective in predicting the stability range.

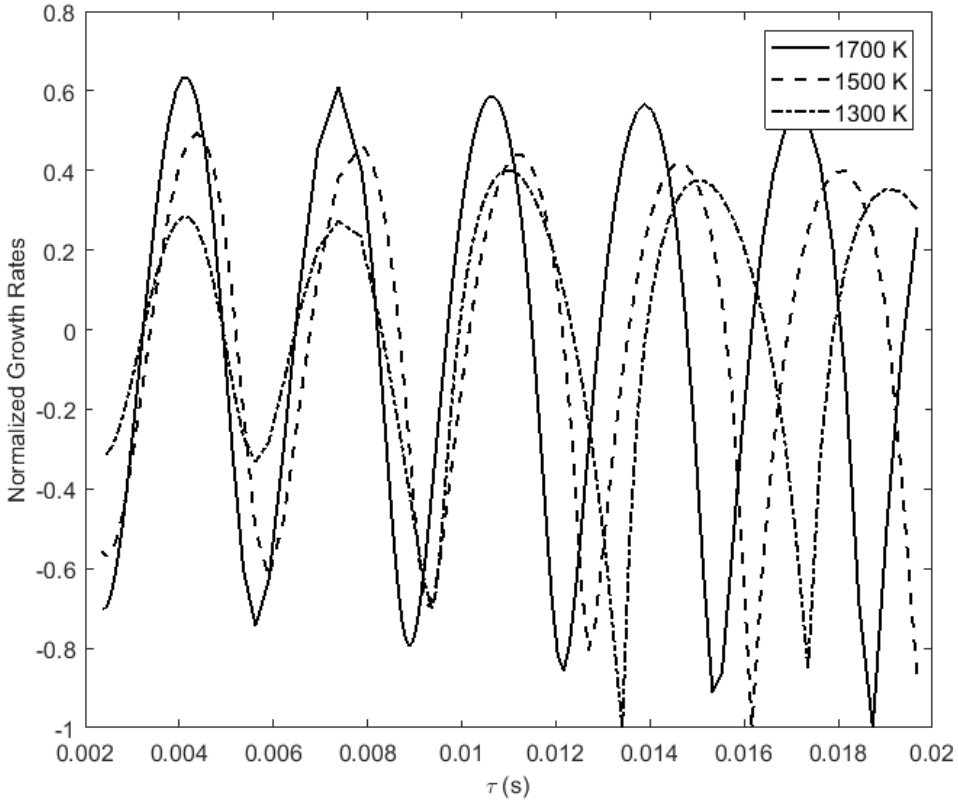

Fig 14: Growth rates predicted by normal n-τ FTF for different temperatures

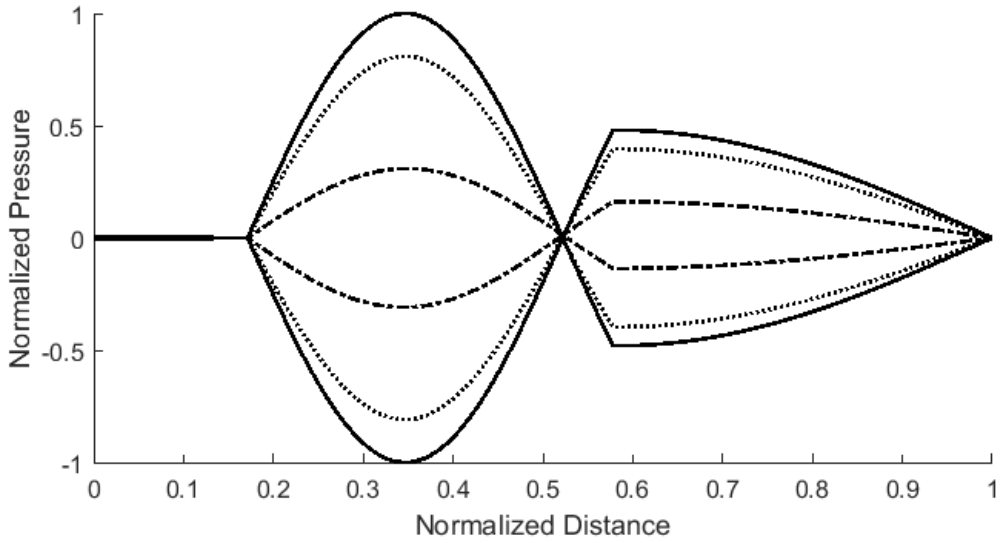

Fig 15: Pressure mode shape predicted by n-τ solver (f = 378 Hz) for a combustion chamber temperature of 1700 K

Statistical Flame Transfer Function Results

Time delay distributions and spatial heat release distributions are extracted from CFD. Fig 16 shows the mean and spread of τ distributions at the flame, which is defined at a progress variable of 0.5. Theoretical mean is the τ calculated from the bulk air and fuel flow rates. The 95% confidence interval, indicated by dashed lines, is calculated based on the standard deviation of τ (σ_τ) about the mean value for different flow rates. The mean of τ values at a particular flow rate closely follows the theoretical mean. The spread of τ values (σ_τ) remains mostly constant for all flow rates.

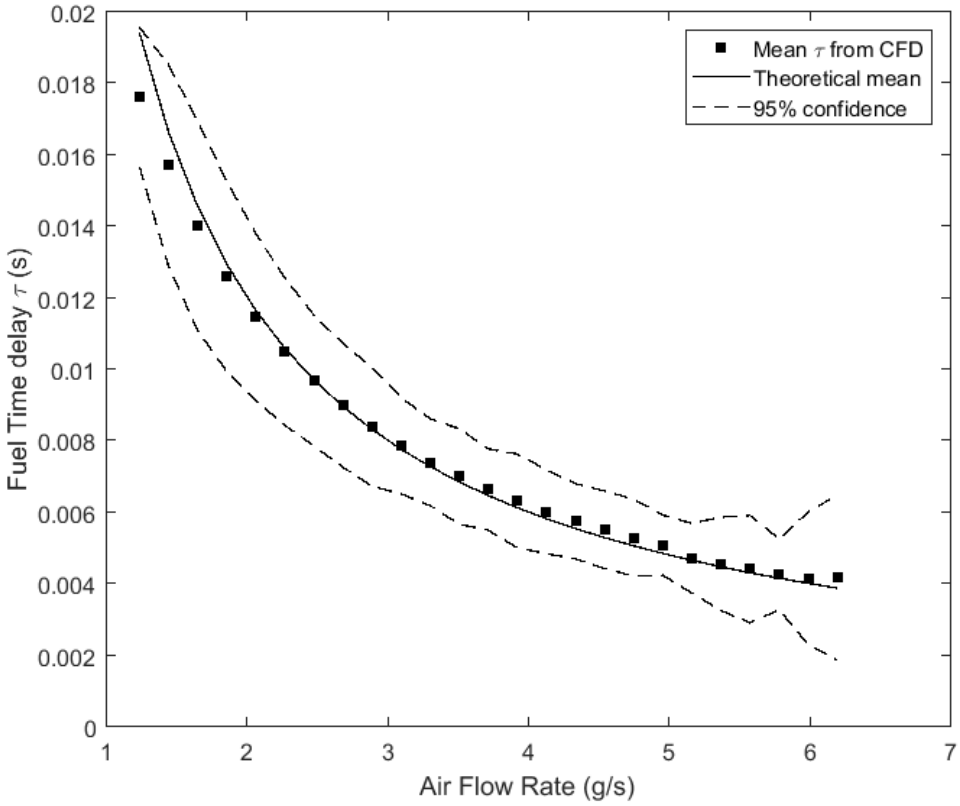

Fig 16: Distribution of convective fuel time delays for different flow rates from CFD

The effects of τ distributions are more pronounced when observed in the context of the stability map. For instance, the 3.51 g/s air flow rate case has a theoretical mean τ delay of 6.7 ms. From CFD, the mean τ of the extracted fuel particles is slightly shifted to 7 ms. The histogram of τ values at c = 0.5 with the mean value (dotted lines) and the growth rates predicted by the solver are shown in Fig 17. When the theoretical mean or the mean of τ distribution is used in the solver, the growth rate predicted is positive, indicating an unstable system for that particular flow rate. However, from the histograms, it is clear that the leftmost bins are closer to the stable part of the stability map. Also, since the probability of fuel particles burning is more biased towards the lower τ values, the stability might shift to the more stable side or be more sensitive to small fluctuations in the bulk flow rate. A

similar τ distribution is observed for all flow rates resulting in a net effect of the entire stability map shifting towards slightly higher τ values.

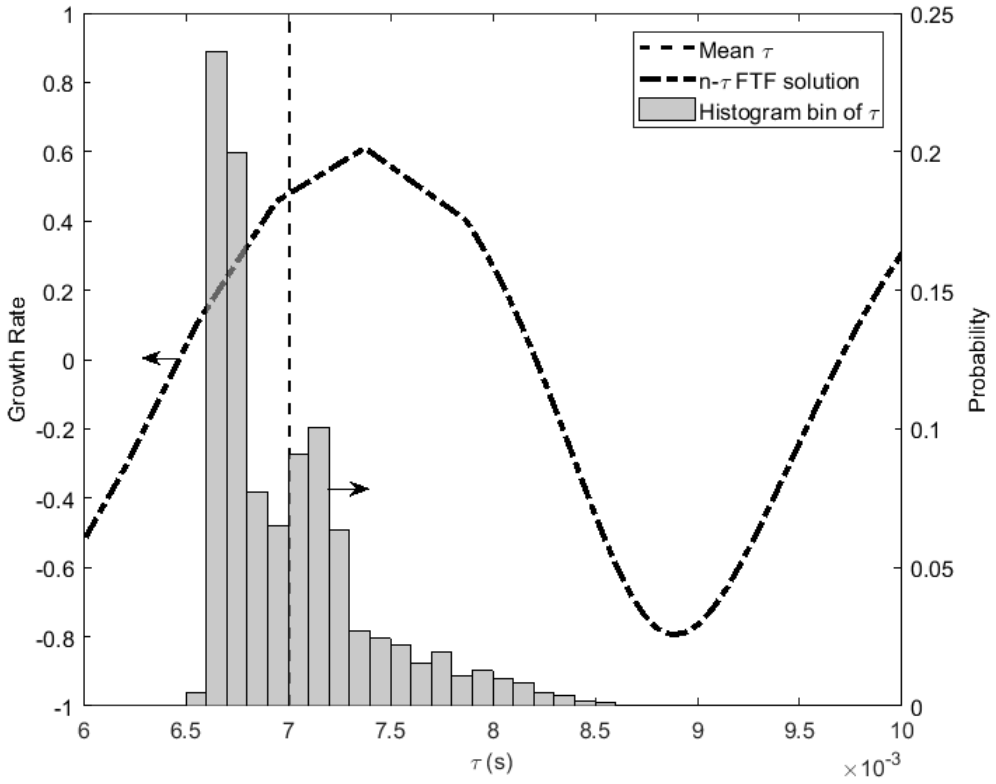

Fig 17: Spread of τ and predicted growth rates for fixed tau values. Dashed vertical line represents the mean of the τ distribution

When the n-τ solver results are compared with the statistical FTF solver's results (Fig 18), some distinct differences between the growth rates can be observed. Once distributions are introduced into the FTF, the τ values at which peak positive growth rates are predicted, are shifted from those by the n-τ FTF. This is evident around the 4 ms and 8 ms fuel time delay ranges (indicated by horizontal arrows 'a'). τ distributions obtained from particle tracking are usually asymmetric (Fig 5 & Fig 17), with the mean τ of the distribution slightly different from that used in the n-τ solver. Therefore, for a given

reactant flow rate, the statistical FTF reflects this bias by shifting the stability map towards higher τ values.

In the τ ranges between the positive peaks, the n-τ FTF consistently predicts a stable system (i.e., negative growth rate). In the statistical FTF, although the magnitude of the predicted growth rates decrease between the peaks, they remain positive even at τ values where maximum negative growths are suggested by the n-τ solver (indicated by vertical arrows 'b'). Since a spatial heat release is considered along with a τ distribution, sections of the flame which contribute positively to the growth rate dampen the sharp fall in predicted growth rates observed in the n-τ solver. The net effect therefore becomes a low magnitude, positive growth rate. Physically, this represents the different sections of the flame that have positive and negative Rayleigh Indices.

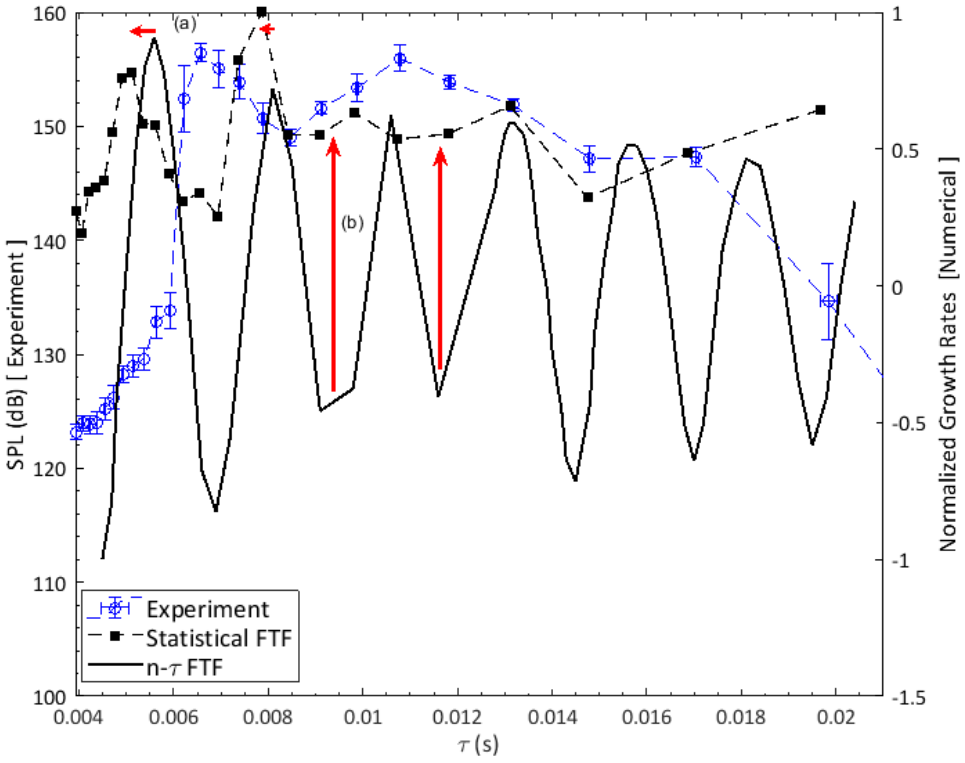

Fig 18: Comparison of growth rates predicted by statistical & n-τ FTFs with experiments

The magnitudes of predicted growth rates can be quantitatively compared with experiments by observing the transient behavior of the system in the linear growth regime. In this study, only a qualitative comparison is performed by observing the limit cycle amplitudes after the system reaches steady state. Although amplitudes at the limit cycle are determined by non-linear processes, the trends in the growth rates determined by the primary driving mechanism (ϕ' in this case) can still be reflected in the limit cycle amplitude (e.g. higher growth rates will contribute to higher limit cycle amplitudes). The pressure amplitudes for a case where most fuel particles reach the flame at a τ most favorable for a positive Rayleigh index would be relatively higher than for one where a larger portion of τ contribute destructively. The experimental pressure amplitudes in the unstable operation region exhibit a trend where a range of relatively low amplitudes exist between two maximum points at τ = 6.5 ms and 11 ms. When compared with the numerical results, the statistical FTF captures this trend in the unstable region much more effectively than the n-τ FTF.

The accuracy of the statistical FTF drops at the higher flow rates (or lower τ delays) where it predicts an unstable system. At higher flow rates, CFD predicts a larger downstream shift in the axial heat release location than that observed in the experiments (Fig 19). At these higher flow rates, the flames start to move further away from the corrugated and wrinkled flamelet regimes. Such flames are not modelled well by the FGM method and more detailed modeling of the flame using detailed chemistry may resolve this issue, but is beyond the scope of the current investigation.

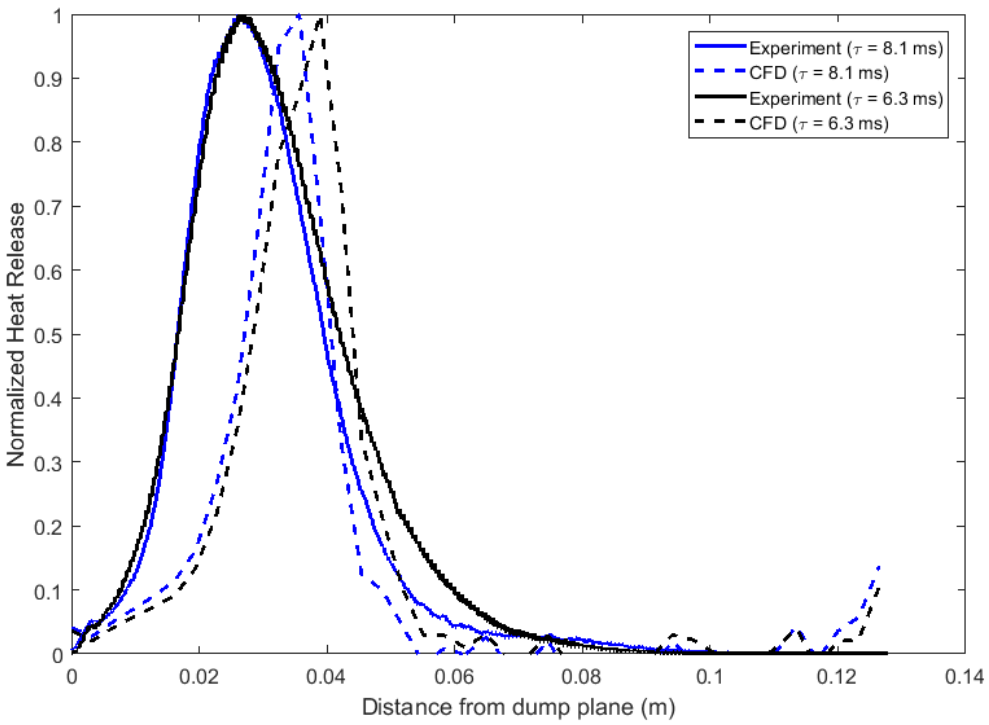

Fig 19: Comparison of axial heat release rate from experiments and CFD

Conclusions

A 1-D thermoacoustic solver capable of making stability predictions using a statistical Flame Transfer Function is developed. The solver is an improvement over existing solvers that use an n-τ FTF in its ability to accept arbitrary distributions in spatial heat release and fuel time delays. Experiments are conducted in an atmospheric pressure combustor where the pressure and heat release in the system are captured via pressure transducers and OH* chemiluminescence imaging, respectively. Raw pressure data is used to reconstruct the pressure wave shape in the combustor. The reconstructed pressure modes validate the mode shapes predicted by the numerical solver. The reconstructed waves are then combined with the OH* chemiluminescence images to generate spatially resolved, line-of-sight integrated Rayleigh Index images. These images identify the regions of the flame which act as thermoacoustic source/sink terms. The volume integrated values from these images are also able to correctly identify the global stability of the system.

The stability predictions of the n-τ model are compared against the experimental observations and are found to be insufficient when the flow is complex. In order to include the effects of flow structures and spatial variations in the heat release, distributions of τ and heat release rates are extracted from RANS simulations. The Flamelet Generated Manifold model was used to model combustion. A modification is made to the n-τ FTF to incorporate the extracted statistical distributions.

However, in the higher flow rates, the FGM flame model does not accurately capture the chemical kinetics, resulting in an inaccurate prediction of the heat release distribution. Better modelling of the flame using detailed chemistry modelling will be able to resolve this issue in future works, widening the range of the statistical FTF to make accurate stability predictions.

Quantification of the heat loss in the combustion chamber can significantly reduce the uncertainty in the actual temperature of the combustion chamber. Since the solver is quite sensitive to the temperature assumption, simulations that include a heat transfer model can significantly improve the model.

In the unstable operating region of the experimental combustor, the statistical Flame Transfer Function method shows improved prediction capabilities when compared to the original n-τ method. The single τ value and flame location assumed by the n-τ model suggests a stable system for multiple fuel time delay ranges in the unstable region. The statistical FTF, is able to correctly predict the instability and also trends in the final limit cycle amplitudes.

References

[1] Lieuwen, T., 2003, "Modeling Premixed Combustion-Acoustic Wave Interactions: A Review," Journal of propulsion and power, 19(5), pp. 765-781.

[2] Lieuwen, T. C., and Yang, V., 2005, Combustion instabilities in gas turbine engines: operational experience, fundamental mechanisms, and modeling, AIAA.

[3] Strutt, J. W., and Rayleigh, B., 1945, The theory of sound, Dover.

[4] Yu, K. H., Trouvé, A., and Daily, J. W., 1991, "Low-frequency pressure oscillations in a model ramjet combustor," Journal of Fluid Mechanics, 232, p. 47.

[5] Kim, K. T., Lee, J. G., Quay, B. D., and Santavicca, D. A., 2010, "The dynamic response of turbulent dihedral V flames: An amplification mechanism of swirling flames," Combustion Science and Technology, 183(2), pp. 163-179.

[6] Schuermans, B., 2003, "Modeling and control of thermoacoustic instabilities,"M.Sc Thesis, École polytechnique fédérale de Lausanne, Lausanne, Switzerland.

[7] Cho, J. H., and Lieuwen, T. C., "Modeling the response of premixed flames to mixture ratio perturbations," Proc. ASME Turbo Expo 2003, collocated with the 2003 International Joint Power Generation Conference, ASME, pp. 67-76.

[8] Renard, P. H., Thévenin, D., Rolon, J. C., and Candel, S., 2000, "Dynamics of flame/vortex interactions," Progress in Energy and Combustion Science, 26(3), pp. 225-282.

[9] Angelberger, C., Veynante, D., Egolfopoulos, F., and Combustion, 2000, "LES of Chemical and Acoustic Forcing of a Premixed Dump Combustor," Journal of Flow and Turbulence, 65(2), pp. 205-222.

[10] Franzelli, B., Riber, E., Gicquel, L. Y. M., and Poinsot, T., 2012, "Large Eddy Simulation of combustion instabilities in a lean partially premixed swirled flame," Combustion and Flame, 159(2), pp. 621-637.

[11] Han, X., Li, J., and Morgans, A. S., 2015, "Prediction of combustion instability limit cycle oscillations by combining flame describing function simulations with a thermoacoustic network model," Combustion and Flame, 162(10), pp. 3632-3647.

[12] Tay Wo Chong, L., Komarek, T., Kaess, R., FöLler, S., and Polifke, W., 2010, "Identification of Flame Transfer Functions From LES of a Premixed Swirl Burner," Proc. ASME Turbo Expo, ASME.

[13] Crocco, L., 1951, "Aspects of Combustion Stability in Liquid Propellant Rocket Motors Part I: Fundamentals. Low Frequency Instability With Monopropellants," Journal of the American Rocket Society, 21(6), pp. 163-178.

[14] Crocco, L., 1952, "Aspects of combustion stability in liquid propellant rocket motors part ii: Low frequency instability with bipropellants. high frequency instability," Journal of the American Rocket Society, 22(1), pp. 7-16.

[15] Dowling, A. P., and Stow, S. R., 2003, "Acoustic analysis of gas turbine combustors," Journal of propulsion and power, 19(5), pp. 751-764.

[16] Selimefendigil, F., and Polifke, W., 2011, "A nonlinear frequency domain model for limit cycles in thermoacoustic systems with modal coupling," International Journal of Spray and Combustion Dynamics, 3(4), pp. 303-330.

[17] Krebs, W., Hellat, J., and Eroglu, A., 2003, "Technische Verbrennungssysteme," Stationäre Gasturbinen, Springer, pp. 447-486.

[18] Poinsot, T., and Veynante, D., 2005, Theoretical and numerical combustion, RT Edwards, Inc.

[19] Kim, K. T., Lee, J. G., Quay, B. D., and Santavicca, D. A., 2010, "Spatially distributed flame transfer functions for predicting combustion dynamics in lean premixed gas turbine combustors," Combustion and Flame, 157(9), pp. 1718-1730.

[20] Smith, K. O., and Blust, J., 2005, "Combustion instabilities in industrial gas turbines: Solar turbines' experience," Combustion Instabilities in Gas Turbine Engines: Operational Experience, Fundamental Mechanisms, and Modeling (2005), AIAA, pp. 29-42.

[21] Scarinci, T., Lieuwen, T., and Yang, V., 2005, "Combustion instability and its passive control: Rolls-Royce aeroderivative engine experience," Combustion Instabilities in Gas Turbine Engines: Operational Experience, Fundamental Mechanisms, and Modeling (2005), AIAA, pp. 65–88.

[22] Mongia, H., Held, T., Hsiao, G., and Pandalai, R., 2005, "Incorporation of combustion instability issues into design process: GE aeroderivative and aero engines experience," Combustion Instabilities in Gas Turbine Engines: Operational Experience, Fundamental Mechanisms, and Modeling (2005), AIAA, pp. 43–63.

[23] Kato, S., Fujimori, T., Dowling, A. P., and Kobayashi, H., 2005, "Effect of heat release distribution on combustion oscillation," Proceedings of the Combustion Institute, 30(2), pp. 1799-1806.

[24] Sattelmayer, T., "Influence of the Combustor Aerodynamics on Combustion Instabilities From Equivalence Ratio Fluctuations," Proc. ASME turbo expo 2000: power for land, sea, and air, ASME.

[25] Armitage, C. A., Riley, A. J., Cant, R. S., Dowling, A. P., and Stow, S. R., 2004, "Flame Transfer Function for Swirled LPP Combustion From Experiments and CFD," Proc. ASME Turbo Expo 2004: Power for Land, Sea, and Air, ASME.

[26] Polifke, W., Kopitz, J., and Serbanoviv, A., 2001, "Impact of the fuel time lag distribution in elliptical premix nozzles on combustion stability," Proc. 7th AIAA/CEAS aeroacoustics conference and exhibit, American Institute of Aeronautics and Astronautics, p. 2104.

[27] Dowd, C. S., and Meadows, J. W., 2018, "Thermoacoustic Instability Model With Porous Media: Linear Stability Analysis and the Impact of Porous Media," Journal of Engineering for Gas Turbines and Power, 141(4), p. 041017.

[28] Levine, H., and Schwinger, J., 1948, "On the Radiation of Sound from an Unflanged Circular Pipe," Physical Review, 73(4), pp. 383-406.

[29] Patil, S., Cooper, J., Orsino, S., Meadows, J., Valdes, R., and Laster, W. R., 2016, "Investigation of Single-Jet Combustor Near Lean Blowout Conditions Using Flamelet-Generated Manifold Combustion Model and Detailed Chemistry," Journal of Engineering for Gas Turbines and Power, 138(12), p. 121503.

[30] Hale, A. A., Cothran, W. D., and Sabo, K. M., "Analysis Technique to Determine the Underlying Wave Structure of Combustion Instabilities From Surface Mounted High Response Static Pressure Sensors," Proc. ASME Turbo Expo 2018: Turbomachinery Technical Conference and Exposition, American Society of Mechanical Engineers, pp. V04AT04A033-V004AT004A033.

[31] Miller, S. J., 2006, "The method of least squares," Mathematics Department Brown University, 114.

[32] Lieuwen, T. C., 2012, Unsteady combustor physics, Cambridge University Press.

Appendix A

Wave Reconstruction Code

```
%   This script reconstructs the wave in the mixing tube or the combustion
%   chamber - 'results.mat' file is required to be in the same folder,
%   where the script is executed
%
% ------------------------------------------------------------------------

%   Load the results.mat file
%   File should contain the data of mics1-3, dpt1,2 - results.mat file
%   generated by the "read_plot_tdms" script can be directly used in this
%   script without any modification. **NOTE:** Sampling frequency is taken
from
%   the results file. Comment and change the sampling rate here or for more
%   permanent changes, change it in the "read_plot_tdms" script.
%
%   The combustion chamber length should be set here, each time it is
%   changed

load results;
%
% Starting index for reconstruction
start_idx = 100;            % to sync start with video at 3000 fps - starts
at 0.001 s (frame 3)
freq_ins =353;             % frequency of instability
%
% Temperature of the duct being reconstructed
T = 1500;                    % K
c_sound = sqrt(1.4*287*T);  % m/s

start_time = start_idx / Fs;
end_time = start_time + (1/freq_ins);
%
% time vector for the selected time period:
t_plot = start_time:(1/Fs):end_time;
% sets the last index, based on the instability frequency:
end_idx = start_idx + floor(Fs / freq_ins);
%
% M - Master Matrix : Each column represents a channel
M =
[mic1_TH(start_idx:end_idx)',mic2_TH(start_idx:end_idx)',mic3_TH(start_idx:en
d_idx)',dpt1_TH(start_idx:end_idx)',dpt2_TH(start_idx:end_idx)'];
%
%
plenum_len = 214.68;        % mm
mixTube_len = 457.25;       % mm
%
% Change Combustion chamber length here:
combchamber_len = 508;      % mm
%
mic1_loc = 452.010;
mic2_loc = 389.572;
mic3_loc = 327.134;
```

```
dpt1_loc = plenum_len+mixTube_len;
dpt2_loc = plenum_len+mixTube_len+combchamber_len-50.8;
%
% Local x-co-ordinates in resprective ducts:
mic1_x = (mic1_loc-plenum_len)/1000;
mic2_x = (mic2_loc-plenum_len)/1000;
mic3_x = (mic3_loc-plenum_len)/1000;
dpt1_x = 0;
dpt2_x = (dpt2_loc-plenum_len-mixTube_len)/1000;
%
% Set the duct being analysed:
%
% Uncomment for mixing tube:

% xdata = [mic3_x,mic2_x,mic1_x,mixTube_len/1000];  %include dpt1
% xdata = [mic3_x,mic2_x,mic1_x];
%
% Uncomment for Combustion Chamber:

xdata = [dpt1_x,dpt2_x,combchamber_len/1000];

%
%x_plt = linspace(0,mixTube_len/1000,80);
x_plt = linspace(0,combchamber_len/1000,80);
%
r2s =0;
FitData = [];
masterMatrix = [];

for t_count=1:length(t_plot)

    % Decide initial guesses:
    if t_count==1
        %   Change this value if the amplitude of Pressure oscillations
        %   deviates a lot from 2000 Pa
        a_guess = 2000 ;
        a = a_guess;
    else
        a_guess = FitData(t_count-1,2);
    end

    % For Mixing Tube:
    ydata = [M(t_count,1:4)];
    %ydata = [M(t_count,1:3)];

    % For CC:
    ydata = [M(t_count,4:5),0];

    % sets the range of the coefficients to search: 'Lower' followed by
    % [a_coeff_lowlim b_coeff_lowlim c_coeff_lowlim].. etc:
    options = fitoptions('Method','NonlinearLeastSquares','Lower',[-Inf -2 -
Inf], ...
        'Upper',[Inf,2,Inf]);

    %   Set the kernel type which is used for the curvefit:
```

```
     f = fittype('a*sin(b*pi*x+c)','options',options);

     %
     % Perform the curve fit, with inital guesses:
    [fit1,gof,fitinfo] = fit(xdata',ydata',f,'StartPoint',[a,1,pi/4]);


    FitData = [FitData; gof.rsquare,coeffvalues(fit1)];

    %% Predicted Curve:

     a = FitData(t_count,2);
     b = FitData(t_count,3);
     c = FitData(t_count,4);

     pred = a .* sin(b.*pi.*x_plt+c);

     % Plot only if the r-square is "decent"
     if FitData(t_count,1)>0.5
         figure(4)
         plot(x_plt,pred,'k');
         hold on;
         plot(xdata,ydata,'s');
         xlabel('x (m)');
         ylabel('Pressure (Pa)');
         ylim([-1000 1000])
     end

    % Store all values at all times
     masterMatrix = [masterMatrix;pred];

end


GrtMax = max(max(abs(masterMatrix)));
LstMax = min(max(abs(masterMatrix)));

% predict the amplitude coefficients
c2_pred = (GrtMax+LstMax)/2;
d2_pred = (GrtMax-LstMax)/2;

c1_pred = c2_pred/2;     % forward travelling
d1_pred = d2_pred/2;     % reverse travelling

kxn = 2*pi*freq_ins/c_sound;  % wave number

[val,max_idx] = max(max(masterMatrix));
phi43_pred = 2*kxn*x_plt(max_idx);

wave_eqn = sprintf('p_1\hat');

disp(['c1 = ' num2str(c1_pred)  ', d1 = ' num2str(d1_pred)]);
disp(['phi_43 = ' num2str(rad2deg(phi43_pred)) ' deg']);
```

```
%% Predicted Pressure equation:

phi3 = deg2rad(30);
phi4 = phi3 - phi43_pred;

t_pred = linspace(t_plot(1),t_plot(end),100);
x_pred = linspace(0,mixTube_len/1000,80);

t_pred2 = 0:(1/Fs):(1/freq_ins);
x_pred = linspace(0,mixTube_len/1000,80);
```

Rayleigh Index Imaging Code

Post Processing of Camera Data:

```
%   The script reads the frames of the video file for the specified number
%   of cycles. The frequency of instability and the frame rate at which the
%   video is captured has to be input.
%
%
%   Name of the video file to be read:
v = VideoReader('20_215_85_C001H001S0001-006.avi');

%   Frequency of the instability (from Pressure data FFT)
ins_freq = 350;     % Hz
%
%   Number of periods to be extracted :
num_cycle = 20;
%
%   Frame rate at which the video is recorded:
fps = 3000;
%
% Number of frames per cycle:
fpc = ceil(fps/ins_freq);
%
%   Calculate the number of frames to be extracted:
no_frames = ceil(num_cycle*fps/ins_freq);

video = read(v,[60 no_frames]);

%   Plotting at different phase angles:

phase_ang = 40:40:360;
phase = 3+ceil(phase_ang./(phase_ang(end))*fpc);
ph = [];

%   Calculate the average intensity in each pixel:
avg_vid = mean(video,4);
%
%   Calculate the average heat release value (only in non-zero pixels):
```

```
[~,ii,v] = find(avg_vid);
%
out_ydir = accumarray(ii,v,[],@mean);
out_all = mean(out_ydir);
%
%   Width:
%   taking pixels whose average is only > 1, the width of the combustion
%   chamber is between pixels 280 and 710. 70 mm/(710-280) = 0.1627 mm/px
%
%   Calculate the total intensity very frame:
sum_int = sum(sum(video,1),2);
sum_int = sum_int(:);
%
% Approximate the width of the combustor in pixels:
sum_yaxis = sum(avg_vid);
% Finds the sum > 200
nz = find(sum_yaxis>200);
% Width:
quartz_width = nz(end)-nz(1);   %in pixels
% resolution:
width_res = quartz_width / 70;     % pixels / mm


%% Plots
cmax = 0;

figure
for p = 1:length(phase)
    subplot(3,3,p)
%     [test,ph] = contourf(video(:,:,:,phase(p)));
%     ph.LineWidth = 0.01;
%     ph.LevelStep = 2;

    imagesc(flipud(video(:,:,:,phase(p))));
    tt = text(600,100, .1, ['\phi = ' num2str(phase_ang(p)) char(176)]);
    tt.Color = [1 1 1];
    colormap(gray)
    axis off;

%     if max(max(ph.ZData))>cmax
%         cmax = max(max(ph.ZData));
%     end

    caxis([0 max(max(max(video)))]);
%     title(['\phi = ' num2str(phase_ang(p)) char(176)]);
end

suptitle('Phase synchronized OH* chemiluminescence');
```

Calculation of RI Images

```
%
%   This script calculates the Rayleigh Index using the Heat release
%   intensity images from OH* chemiluminescence (testCameraPost.m) and the
%   recontructed pressure in the combustion chamber (wave_cc.m). Both of
```

```
%   these scripts should be run before running this script.

%   video : xpixel,ypixel,zpixel,frame
%   first cycle: 3rd frame
%
% Convert uint8 matrix to a single precision double - required for
% interpolation to work
testvid = single(testvid);

%% Interpolation
%
%   To multiply the pressure osciallations and the heat release
%   osciallations, both these quantities should be known at the same
%   instant - therefore, the available frames from chemiluminescence images
%   are interpolated to approximate the heat release at a higher
%   'pseudo-frame rate'
%

% No of frames in the testvid:
no_frames = 60;
start_frame = 60;
frame_per_cycle = 9;
no_pr_data_per_cycle = 285;
% meshgrid of X,Y co-ordinates and Original Time vector
[X,Y,T] =
meshgrid(1:1024,1:1024,linspace(start_frame/3000,(start_frame+frame_per_cycle
)/3000,frame_per_cycle));
% Query co-ordinates and Time vector
[Xq,Yq,Tq] =
meshgrid(1:1024,1:1024,linspace(start_frame/3000,(start_frame+frame_per_cycle
)/3000,no_pr_data_per_cycle));
% Interpolated Values:
Vq = interp3(X,Y,T,testvid(:,:,1:9),Xq,Yq,Tq);

% sum of intensities of the queried points; cast into vector form
s_i_q = sum(sum(Vq,1));
s_i_q = s_i_q(:);
%

% Cast queried time in vector form
Tq_vec = Tq(1,1,:);
Tq_vec = Tq_vec(:);

%% Calculate Rayleigh Index

m_q = mean(Vq,3);       % mean intensity in each pixel
%
% Perturbation heat release:
Vq_p = Vq - m_q;
%
% Calculate Pressure at each pixel
%
%   From testCameraPost, the resolution is 0.1628 mm/px, based on which,
%   the x array is created to calculate the Rayleigh index.
```

```
x_ri = ([1:1024] * 0.1628 / 1000);
%
%   Calculate the pressure at each pixel (assuming pressure to be 1D) using
%   the curvefit-coefficients "FitData" at each time step.

 p_ri = FitData(:,2) .* sin(FitData(:,3).* pi .* x_ri + FitData(:,4));
%

for c = 1:285
    p_ri_2D(:,:,c) = p_ri(c,:)' .* ones(1024,1024);
end

ip_ri = Vq_p .* p_ri_2D;

%   Calcualte the RI
tv = linspace(0.001,11/3000,285);
tic
for xi=1:1024
    %disp([num2str((xi-1)/1024*100) ' % done...']);
    for yi=1:1024
        tt = ip_ri(xi,yi,:);
        tt = tt(:);
        ri(xi,yi) = 1/(11/3000 - 0.001) * trapz(tv,tt');
    end
end
h = toc;
% using threshold, create a BW image:
ri_bw = im2bw(ri,0);

%% Plots
figure
subplot(1,2,1)
imagesc(flipud(ri));
pbaspect([1 1 1]);
%colorbar;

subplot(1,2,2)
imshow(flipud(ri_bw));
pbaspect([1 1 1]);
```

Statistical FTF Solver

Inputs script:

```
%% Iterate for different flow rates
for flowr = 300:-10:60


    clearvars -except flowr;

    tic;
    % Define the number of flames and the number of bins for \tau
    % distribution in each of the flame
    n_flames = 5;
```

```
    n_tau_bins = 5;
    % Load heat release matrix
    load ../hrr.mat;

    syms t f; % for integration (tau distibution contribution)

    % Co-ordinates of the dump plane - to calculate \tau and FlameLocation
    dp_offset_in = 6.81; % inches - from start of domain
    dp_offset = dp_offset_in * 0.0254;
    % Set general Properties for the solver:
    R = 286.9;
    % Number of ducts before splitting the flames
    nDuctsActual = 4;

    % Speaker box and mixing tube:
    DuctLength = [0.2146863 0.51003];
    CombChamberLen = 0.529;
% --------------------
    % Temperature of the combustion chamber
    Temp_cc = 1700;     %K

    disp(flowr);
    % flow rate count
    frcount = (flowr-40)/10+1;
    %disp(frcount)
    %
    % Load the mat files which contain the tau data of the particle tracks
    % for the current flow rate:
    load(sprintf('../bins_mod_%d',flowr));
    clearvars int;

    % Set global interaction index (n) value
    tot_n = -0.1;

    tau_contrib = [0 0];

    % capture bulk of the flame
    [maxval,maxid] = max(hrr(frcount,:));

    [minmin,minminid] = min(hrr(frcount,1:maxid));
    [minmax,minmaxid] = min(hrr(frcount,maxid:maxid+12));
    minmaxid = minmaxid + maxid - 1;

    xxq = linspace(xx(minminid),xx(minmaxid),n_flames+1);
    vq = interp1(xx(minminid:minmaxid),hrr(frcount,minminid:minmaxid),xxq);


    if xx(minmaxid) < max(burnt_avg(:,4))
        maxbinval = max(burnt_avg(:,4));
    else
        maxbinval = [];
    end

    edges2 = [0 linspace(xx(minminid),xx(minmaxid),n_flames+1) maxbinval];
```

```
    [N_flamebin] = histcounts(burnt_avg(:,4),edges2);
    h2{frcount}{1} = N_flamebin;
    h2{frcount}{2} = edges2;

    A = discretize(burnt_avg(:,4),edges2);

    comboMat = [burnt_avg A];

    % For each flame, calculate the tau contribution and the flame
    % interaction index contributiont to the overall Oj matrix
    for flameNo=1:n_flames
        n(flameNo) = (trapz(xxq(flameNo:flameNo+1),vq(flameNo:flameNo+1)) /
trapz(xxq,vq)) * tot_n;

         f_tau_group{flameNo} = comboMat(comboMat(:,5)==flameNo,:);

             if ~isempty(f_tau_group{flameNo})
                 [Val,TauEdges] =
histcounts(f_tau_group{flameNo}(:,4),n_tau_bins);
                 P = Val ./ sum(Val);
             else
                 tau_contrib = [tau_contrib 0];
             end

       if ~isempty(f_tau_group{flameNo})
         for tauBin=1:n_tau_bins


bin_int(tauBin)=int(exp(1i*2*pi()*f*t),t,TauEdges(tauBin+1),TauEdges(tauBin))
;
            hgt(tauBin)=(bin_int(tauBin)*P(tauBin))/bin_width;
         end

       tau_contrib = [tau_contrib sum(hgt)];
       end

       % calculate the co-ordinates of the start and the end of the flame

    end

    % temporary duct lengths
    DL_temp = edges2(2:1+n_flames) - dp_offset;
    DL_cc = [DL_temp(1) diff(DL_temp)];
    CC_LenAfterFlames = CombChamberLen - DL_temp(end);

    DuctLength = [DuctLength,DL_cc,CC_LenAfterFlames];
    nDucts = length(DuctLength);
    %
    % Areas of cross section
    S = [0.04837176,0.000159,ones(1,n_flames).*0.003848,0.003848];

    k_rat = ones(1,nDucts).*1.4;
    Patm = ones(1,nDucts).*101325;
```

```
    Temp = [300,300,ones(1,nDucts-2).* Temp_cc];

    co = sqrt(k_rat.*R.*Temp); %Speed of Sount (m/s) *Gamma is constant
    rho = Patm.*k_rat./co.^2; %Density (kg/m3) *Ideal Gas Assumption

    h = ones(1,nDucts).*1;
    Sigma = ones(1,nDucts).*0;
    Struct = ones(1,nDucts).*1;
    Kappa = ones(1,nDucts).*141855;

    IntIndex = [0 0]; % between speaker box - mixing tube - dump plane
    IntIndex = [IntIndex,n];

    % Run script to solve
    Final_CombinedSolver.m;

    timeTaken = toc;
%     save(sprintf('combined_Results_%d.mat',flowr));
    save(sprintf('combined_eqn_nMinus1_Results_%d_%d_K.mat',flowr,Temp_cc));

end
```

Solver and support functions:

```
format short
i = sqrt(-1);
% Reference to Poinsot Textbook is Theoretical and Numerical Combustion 2nd
% Edition by Thierry Poinsot and Denis Veynante
%% Initialization and Inputs

% Commented for multiple flames
RJ = -1; %Reflection Coefficent - R = 1:Closed -1:Open
R1 = 1;
R = 286.9; %Gas Constant (J/kgK) ***Constant***


for dd = 1:1:nDucts %Builds the global x distance variable x1
    DuctEnds(1) = 0;
    DuctEnds(dd+1) = DuctEnds(dd)+DuctLength(dd);  % x1 - starting x co-ord
of duct,
end

% ------------------------------------------------------------------------
%% Solution of Global Matrix for Frequency
G{1} = [1,0;0,1]; %Identity Matrix so that G(1) = T1
%
% Already defined in combined_tauContribution
%syms f
for yy=1:1:nDucts %Defined in Ch. 7 of Foundatations of Engineering Acoustics
    k_new(yy)=
sqrt(((2*pi()*f)^2)*(Struct(yy)*rho(yy)/Kappa(yy))+i*Sigma(yy)*h(yy)*2*pi()*f
/Kappa(yy));
    %With nominal values for h, Struct, Kappa and Sigman, this equation
    %reduces to k =w/c
```

```
end
for q = 1:1:nDucts-1 %Loops through interfaces to build Gamma, T, and G
matricies
    %Gamma(q)= rho(q+1)*co(q+1)*S(q)/(rho(q)*co(q)*S(q+1)); % Solves section
parameter for each duct
    %Section Parameter defined in Poisnot Textbook Ch.8
    Gamma(q) = S(q)*Kappa(q+1)*k_new(q+1)/(S(q+1)*Kappa(q)*k_new(q));
    for col = 1:2 %Column loop
        for row = 1:2 %Row loop
            T{q}(row,col) = 0.5*exp((-
1)^(1+col)*i*k_new(q)*DuctLength(q))*(1+(Gamma(q)*(-1)^(row+col)));
        end
    end
    G{q+1} = T{q}*G{q}; %Global Matrix build => Tn*Tn-1*Tn-2...T2*T1 //
T3*(T2*T1) = (T3*T2)*T1
end
Amp{1} = [R1,1];
PrevIntIndex = IntIndex;
IntIndex = zeros(1,nDucts-1);

% First time run - assuming no flame (to get approxmiate frequency)
% Second time run assuming flame
for gg = 1:1:2
    for ii =1:1:nDucts-1
        %Establishing Oj matrix for heat release terms - Defined in Poinsot

        % IntIndex accounts for the spatial distribution
        % tau_contrib adds the tau contribution
        O{ii}(1) =
0.5*h(ii)*Gamma(ii)*IntIndex(ii)*tau_contrib(ii)*(Amp{ii}(1)*exp(i*k_new(ii)*
DuctLength(ii))-Amp{ii}(2)*exp(-i*k_new(ii)*DuctLength(ii)));
        O{ii}(2) = -
0.5*h(ii)*Gamma(ii)*IntIndex(ii)*tau_contrib(ii)*(Amp{ii}(1)*exp(i*k_new(ii)*
DuctLength(ii))-Amp{ii}(2)*exp(-i*k_new(ii)*DuctLength(ii)));

        %Loops to define summation term used for determining frequency and
        %amplitueds - Poinsot Textbook Ch. 8.4
        if ii == 1
            CombTerm1{ii}(1) = O{ii}(1);
            CombTerm1{ii}(2) = O{ii}(2);
        else
            Sum{1}=[1,0;0,1];
            ComboSum{1} = zeros(2,1);

            for kk = 1:1:(ii-1)
                Sum{kk+1} = Sum{kk}*T{ii-(kk-1)};
                ComboSum{kk+1} = Sum{kk+1}*[O{ii-kk}(1);O{ii-
kk}(2)]+ComboSum{kk};
            end
            CombTerm1{ii} = ComboSum{kk+1}+[O{ii}(1);O{ii}(2)];
        end
        Amp{ii+1}(1) =
G{ii+1}(1,1)*Amp{1}(1)+G{ii+1}(1,2)*Amp{1}(2)+CombTerm1{ii}(1);
        Amp{ii+1}(2) =
G{ii+1}(2,1)*Amp{1}(1)+G{ii+1}(2,2)*Amp{1}(2)+CombTerm1{ii}(2);
    end
```

```
    %% Solving for the frequency and Amplitude values ***Assuming A1- is
equal to 1***
    %Using second boundary conditions - RJ = AJ+/AJ-*exp(2ikJ*xJ)
    Init_Guess{1} = 0;
    eqn = (Amp{end}(1)/Amp{end}(2))*exp(2*i*k_new(end)*DuctLength(end))-RJ;
    disp('running findZeros...');
    soln = findzeros(eqn,[1-Inf*i 1000+Inf*i]);
    disp('running VPAsolve...');
    soln2 = vpasolve(eqn,f,Init_Guess{gg});
    Init_Guess{2} = soln(1); %***Set mode here***
    IntIndex = PrevIntIndex;
    %double(Init_Guess{2})
end
disp('calculating freq');
freq = soln2;

% Uses Dr. Meadows findzeros function to find all points in range which eqn =
0. Different modes.
% Have to specify the rectangle in the complex domain for which the search
% will take place within. Imaginary Range was causing issues so is reset
% each time in the findzeros function to look between +- Infinity
for ii = 1:1:nDucts
    Amp{ii} = subs(Amp{ii},f,freq);
end

function sol = findzeros( f,range,err )
    if nargin < 3                                % If number of arguments is
less than 3
        err = 1e-3;                              % Set default value for error
    end
    %sol = real(vpasolve(f,range))
    sol = vpasolve(f,range);

    if(isempty(sol))
        return
    else
        %sol = vpasolve(f,[sol-10i, sol+10i]);
        lowLimit = real(sol-err)+Inf*i;
        highLimit = real(sol+err)-Inf*i;
        temp = findzeros(f,[range(1) lowLimit],1);
        if ~isempty(temp)
            sol = sort([sol temp]);
        end
        temp = findzeros(f,[highLimit range(2)],1);
        if ~isempty(temp)
            sol = sort([sol temp]);
        end
        return
    end
end
```